Univerzita Karlova v Praze
Matematicko-fyzikální fakulta

DIPLOMOVÁ PRÁCE

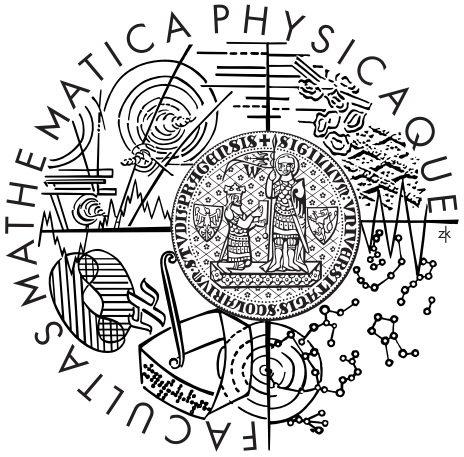

Martin Zahradník

Studium fyzikálních vlastností magnetických oxidů spektroskopickými metodami

Fyzikální ústav UK

Vedoucí diplomové práce: RNDr. Martin Veis, Ph.D.
Studijní program: Fyzika
Studijní obor: Optika a optoelektronika

Praha 2014

First of all, I would like to thank to my supervisor RNDr. Martin Veis, Ph.D. for all his precious help and advice concerning both my studies and master thesis. His patience and kindness as a teacher and supervisor is exceptional.

I am very thankful to doc. RNDr. Miroslav Kučera, CSc. for sharing his knowledge about magneto-optical Faraday spectroscopy as well as for his help with experimental measurements and theoretical analyzes of Faraday effect.

Great thanks are addressed to Mgr. Jan Mistrík, Ph.D. for his essential help with ellipsometry measurements and analyzes.

I thank to research group of Prof. Philippe Lecoeur for preparation of high quality $La_{2/3}Sr_{1/3}MnO_3$ films and also to research group of Prof. Caroline A. Ross for preparation of $Ce_{1-x}Co_xO_{2-\delta}$ films.

I would also like to thank to employees and students of the division of magneto-optics: RNDr. Roman Antoš, Ph.D., RNDr. Eva Jakubisová, Ph.D., Mgr. Eva Jesenská, Mgr. Martin Hanuš and Mgr. Zuzana Onderišinová. Their help and support in our laboratory was many times important for me.

Special thanks belong to my parents, my brother and friends for overall support during my studies, which was always helping me to overcome all difficulties.

I am exceptionally thankful to Siria, my girlfriend, for everything.

I declare that I carried out this master thesis independently, and only with the cited sources, literature and other professional sources.

I understand that my work relates to the rights and obligations under the Act No. 121/2000 Coll., the Copyright Act, as amended, in particular the fact that the Charles University in Prague has the right to conclude a license agreement on the use of this work as a school work pursuant to Section 60 paragraph 1 of the Copyright Act.

In Prague 31. 7. 2014

Název práce: Studium fyzikálních vlastností magnetických oxidů spektroskopickými metodami

Autor: Martin Zahradník

Katedra: Fyzikální ústav UK

Vedoucí diplomové práce: RNDr. Martin Veis, Ph.D., Fyzikální ústav UK

Abstrakt: V této práci byly studovány dvě skupiny magnetických oxidů. Tenké vrstvy $La_{2/3}Sr_{1/3}MnO_3$ (LSMO) deponované pulsní laserovou depozicí (PLD) na substrátech $SrTiO_3$ (STO) byly charakterizovány pomocí polární a longitudinální magnetooptické (MO) Kerrovy spektroskopie. Experimentální výsledky byly porovnány s teoretickými výpočty založenými na Yehově maticovém formalismu. Velmi dobrá shoda mezi experimentálními a teoretickými daty svědčí o vysokém magnetickém uspořádání až do tloušťky vrstev 5 nm a také o mechanismu potlačení interakce dvojité výměny poblíž rozhraní LSMO/STO. Magneticky dopované vrstvy $Ce_{1-x}Co_xO_{2-\delta}$ deponované pomocí PLD na substrátech MgO (x = 0.05 a 0.10) a Si (x = 0.20) byly studovány pomocí spektroskopické elipsometrie a MO Faradayovy a Kerrovy spektroskopie. Byla získána spektra diagonálních i nediagonálních prvků tenzoru permitivity, která byla ověřena teoretickými výpočty porovnanými s experimentálními daty. Diagonální spektra odhalila dva optické přechody z O $2p$ do Ce stavů. Nediagonální spektra odhalila dva paramagnetické přechody zahrnující kobaltové ionty. Byl pozorován zásadní vliv kobaltového dopování na výsledné feromagnetické vlastnosti CeO_2.

Klíčová slova: magnetooptický Kerrův efekt, Faradayův efekt, pulsní laserová depozice, LSMO, kobaltem dopované oxidy ceru

Title: Study of physical properties of magnetic oxides using spectroscopic techniques

Author: Martin Zahradník

Department: Institute of Physics of Charles University

Supervisor: RNDr. Martin Veis, Ph.D., Institute of Physics of Charles University

Abstract: Two groups of magnetic oxides were investigated in this thesis. Thin films of $La_{2/3}Sr_{1/3}MnO_3$ (LSMO) deposited by pulsed laser deposition (PLD) on $SrTiO_3$ (STO) substrates were characterized by polar and longitudinal magneto-optical (MO) Kerr spectroscopy. Experimental results were compared to theoretical calculations based on the transfer matrix formalism. A very good agreement between experimental and theoretical data revealed high magnetic ordering down to 5 nm of film thickness as well as a mechanism of suppression of double exchange interaction near the LSMO/STO interface. Magnetically doped $Ce_{1-x}Co_xO_{2-\delta}$ films deposited by PLD on MgO (x = 0.05 and 0.10) and oxidized Si (x = 0.20) substrates were studied by combination of spectroscopic ellipsometry and MO Faraday and Kerr spectroscopy. Both diagonal and off-diagonal permittivity tensor components were obtained and verified by theoretical calculations confronted with experimental data. Diagonal spectra revealed two optical transitions from oxygen to cerium states. Off-diagonal spectra revealed two paramagnetic transitions involving cobalt ions. An essential influence of cobalt doping on the resulting ferromagnetic properties of CeO_2 was observed.

Keywords: magneto-optical Kerr effect, Faraday effect, pulsed laser deposition, LSMO, cobalt doped cerium oxides

Contents

Introduction

This thesis is devoted to the systematic study of physical propertied of two different magnetic oxides. Each material has different potential application. The first material belongs to the group of materials which are promising for applications in spintronics due to its high degree of spin polarization. Such materials act as conductors for one spin orientation and isolators for another. Among these materials mixed valence manganese oxides are promising candidates. Their Curie temperature is higher than the room one ($T_{C,bulk} \sim 370$ K) [36] which makes them promising for room temperature device applications. The most well known example of application is probably a magnetic field sensor based on tunnel magnetoresistance. Two ferromagnetic materials are separated by a thin insulating layer which allows electrons to tunnel through the barrier from one ferromagnet into another. Applying of an external magnetic field allows us to change the direction of magnetization in the ferromagnetic layers. There is a significantly higher probability of tunnelling through the barrier at parallel orientations of the directions of magnetization than at the antiparallel one. This phenomenon is employed in reading heads of hard disk drives or magnetoresistive random-access memory (MRAM).

A schematic drawing of MRAM chip is together with basic principle of data storage and reading is shown in Fig. 1. The function is based on the distinct probability rates of tunneling through the insulating barrier at different orientations of the magnetization in each ferromagnetic layer. This can be measured as electrical resistance and therefore the logical zero and one can be recognized. Because of the need to control the magnetization, there is a seek for ferromagnetic materials with proper physical properties suitable for desired miniaturization and other construction requirements.

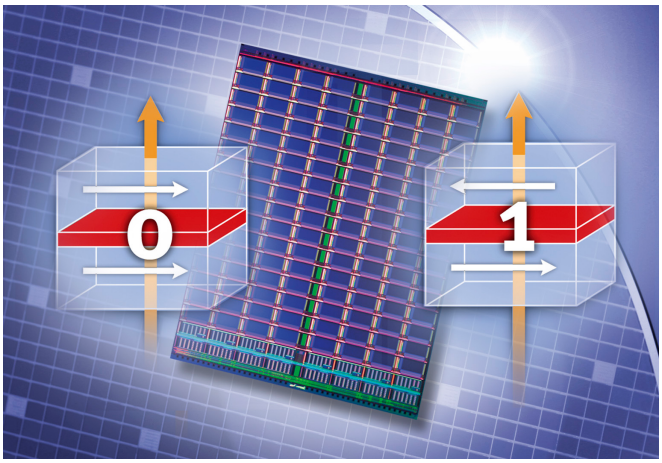

Figure 1: A chip of MRAM with schematic representation of logical zero and one.

Promising materials in this research field have appeared to be ferromagnetic mixed valence manganese oxides. They exhibit colossal magnetoresistence (CMR). This property allows them significantly change their electrical resistance in presence of an external magnetic field. This phenomenon was first experimentally observed in different manganese oxides [36, 74] and then theoretically

explained by C. Zener [86] via double-exchange (DE) interaction - a "double" electron transition between manganese cations via oxygen ion. Probability of such transitions is influenced by Mn^{3+}-O-Mn^{4+} geometry (bond lengths, bond angle), therefore an important factor for their ferromagnetic properties is a strain arising due a to lattice mismatched substrate used for deposition. Magneto-optical (MO) spectroscopy is then a valuable tool for the investigation of ultrathin layers of these materials where the undesired strain has the strongest influence.

Research of the second group of the magnetic oxides has been motivated by recent proposals of new device concepts using MO phenomena, e.g. MO isolators [7] or magneto-photonic crystals [30]. A recently fabricated MO isolator is shown in Fig. 2. It consists of SiO_2 substrate layer, which is etched in order to deposite Si waveguide resonator inside. Top of this structure is covered with a MO layer. A light wave of given wavelength propagating through the optical waveguide experiences different absorption when magnetization of different direction is applied in the MO layer.

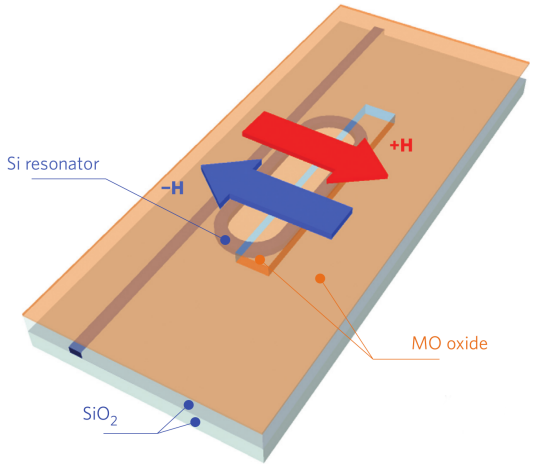

Figure 2: Schematic diagram of MO isolater [7].

These novel concepts, which are employing on-chip integrated structures of nanometer scale, are encouraging search for new materials, which would enable their practical realization. Not only MO effects large enough are sufficient for their widespread exploitation, there are several other technological issues needed to be overcome.

One of these important factors is compatibility with silicon technology. From this point of view there is a highly interesting material - magnetically doped CeO_2 - which shows excellent silicon compatibility [70]. Moreover it exhibits high Curie temperature making it promising for room temperature device applications. Its properties can be tuned by Co doping [8] but detailed optical and MO description of Co doped CeO_2 is still missing as well as better understanding of the origin of its ferromagnetic properties. Therefore MO spectroscopy combined with spectroscopic ellipsometry can provide a useful tool for obtaining more detailed knowledge about optical and MO properties of these materials.

The main goals of this thesis are on one hand to solve both individual problems - to analyse interface phenomena occurring in $La_{2/3}Sr_{1/3}MnO_3$ (LSMO) ultrathin layers grown on $SrTiO_3$ (STO) substrate and to investigate influence of Co doping

on resulting properties of CeO_2, on the other hand we also try to demonstrate distinct possible usages of magneto-optical characterization techniques. In the first case we perform an analysis of the structure, providing depth sensitive picture of ferromagnetic properties of the investigated material, and concluding some information about the layer growth and its electronic structure. In the second case we are focused more on phenomenological description of the studied material and its optical and MO properties, in other words obtaining its material parameters - components of the permittivity tensor.

Besides obtained results, the first two chapters contain short theoretical background for better understanding of the essential phenomena. Third chapter describes the experimental techniques which were used to obtain experimental data. Fourth chapter contains detailed description of the investigated samples and their preparation. Finally, fifth chapter contain the experimental results.

1. Light polarization and magneto-optical angles

1.1 Light polarization

Because we consider light as an electromagnetic wave, we can describe some of its properties by simple description of the wave motion. Its electric component is dominating in the interaction of light with matter, therefore we use the vector of electric field strength to define the polarization of light, which is given by the time evolution of this vector at a given point in space. If we suppose the light to be a time-harmonic plane wave consisting of three independent oscillations alongside the Cartesian axes, it can be shown [2] that the electric field strength vector traces an ellipse. In other words that the most general case of light polarization is an elliptic polarization. The ellipse of polarization (Fig. 1.1) takes place in a plane perpendicular to the wave vector. In Fig. 1.1 we depict an example of the wave travelling along the z axis, looking against the direction of propagation. The ellipse is uniquely determined by four parameters but for the characterization of the polarization state only two of them are necessary. As shown in Fig. 1.1, they are

- the azimuth θ - an oriented angle between the major axis of the ellipse and positive x axis, it determines the orientation of the ellipse in its plane and it ranges from $-\frac{\pi}{2}$ to $\frac{\pi}{2}$, and
- the ellipticity e - a ratio of the lengths of the semi-minor and the semi-major axes, $e = \frac{b}{a}$. Its values are in the interval $-1 \leq e \leq 1$. According to the sign of the ellipticity we assign a handedness to the polarization state, positive sign corresponds to a right-handed polarization, negative sign to a left-handed one. What we actually see while looking against the direction of propagation is a clockwise motion of the electric field vector in case of the right-handed polarization and anti-clockwise motion in case of the left-handed one. A quantity ϵ defined by the relation $e = \tan\epsilon$ is called ellipticity angle and according to the values of the ellipticity it ranges from $-\frac{\pi}{4}$ to $\frac{\pi}{4}$.

The other two quantities not necessary for defining the polarization state are the amplitude A and the absolute phase δ_0. The former is given by the axes of the ellipse as $A = \sqrt{a^2 + b^2}$ and is related to the intensity I by equation $I = \boldsymbol{E}^\dagger \boldsymbol{E} = A^2 = a^2 + b^2$, where $\boldsymbol{E}$ is the electric field strength and $\dagger$ denotes a Hermitian conjugate. The latter gives an information about the initial state, it is an angle between the electric field vector in time $t = 0$ and the major axis of the ellipse, therefore it ranges from $-\pi$ to π.

1.2 Jones calculus

There are various approaches for the description of polarized light. For our purposes we will introduce Jones calculus [2] employing completely polarized light.

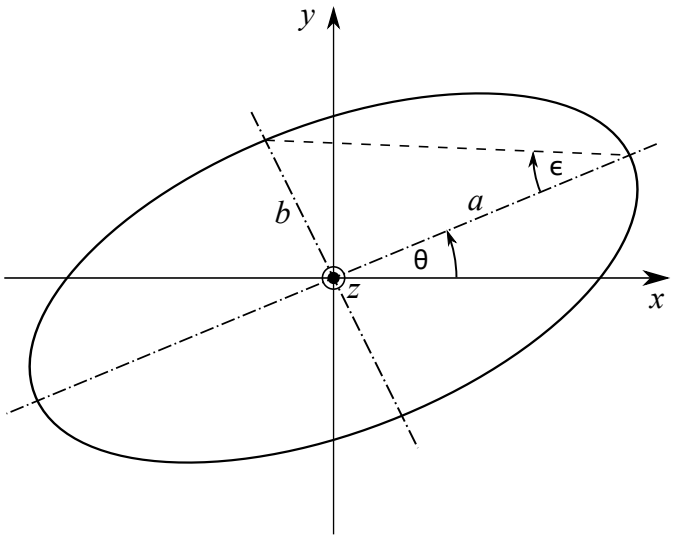

Figure 1.1: The ellipse of polarization while looking against the direction of propagation of the light wave.

The light is represented by Jones vectors and optical elements by Jones matrices which allows us easily calculate the polarization state of light passed through an optical system.

Let us have a completely polarized monochromatic plane wave propagating alongside the z axis as in the previous section. It can be expressed as a superposition of two components oscillating in the directions of x and y axes having amplitudes A_{0_x}, A_{0_y} and absolute phases δ_x, δ_y. As was already mentioned we do not need these quantities for the description of the polarization state, therefore after introducing $\tan\alpha = \frac{A_{0_y}}{A_{0_x}}$ and phase shift $\delta = \delta_y - \delta_x$ we can define normalized Jones vector as

$$\boldsymbol{J} = \begin{bmatrix} \cos\alpha \\ \sin\alpha e^{i\delta} \end{bmatrix} = \cos\alpha \boldsymbol{J}_x + \sin\alpha e^{i\delta}\boldsymbol{J}_y, \tag{1.1}$$

where we use the Cartesian basis of linear polarizations $\boldsymbol{J}_x$ and $\boldsymbol{J}_y$ given as

$$\boldsymbol{J}_x = \begin{bmatrix} 1 \\ 0 \end{bmatrix}, \qquad \boldsymbol{J}_y = \begin{bmatrix} 0 \\ 1 \end{bmatrix}. \tag{1.2}$$

Since we have mentioned that for the description of polarization only azimuth and ellipticity (eventually ellipticity angle) of the polarization ellipse are necessary, we should explain their relations to newly introduced quantities α and δ, which are [2]

$$\tan 2\theta = \tan 2\alpha \cos\delta, \tag{1.3}$$

$$\sin 2\epsilon = \sin 2\alpha \sin\delta. \tag{1.4}$$

Now we have described the polarized light wave and we need to find out how the polarization changes while passing through the optical system. In Jones calculus, any transmission or reflection element which affects the polarization of the wave can be characterized by 2×2 matrix. First we take a look at the reflection elements. Let us consider two coordinate systems $\mathrm{S}^{(I)}$ and $\mathrm{S}^{(R)}$ as shown in the Fig. 1.2. The direction of x axes is perpendicular to the plane of incidence,

we call the light linearly polarized in this direction as s-polarized (from German *senkrecht* - perpendicular) while the direction of y axes is parallel to the plane of incidence and the light linearly polarized in this direction is called p-polarized. In case of normal light incidence this distinction becomes insignificant. The

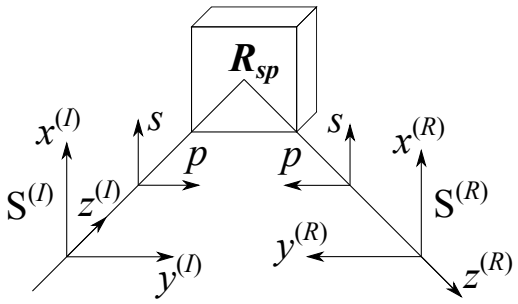

Figure 1.2: Reflection optical element with coordinate systems of the incident and reflected wave.

polarization of an incident wave is in the system $\mathrm{S}^{(I)}$ characterized by Jones vector $\boldsymbol{J}^{(I)}$ and reflected wave is in the system $\mathrm{S}^{(R)}$ described by a Jones vector $\boldsymbol{J}^{(R)}$. Both vectors are connected by a transformation which can be written in a matrix form

$$\boldsymbol{J}^{(R)} = \boldsymbol{R}_{sp} \cdot \boldsymbol{J}^{(I)}, \tag{1.5}$$

where the Jones reflection matrix

$$\boldsymbol{R}_{sp} = \begin{bmatrix} r_{ss} & r_{sp} \\ r_{ps} & r_{pp} \end{bmatrix} \tag{1.6}$$

characterizes a change of the polarization state of the light wave when reflecting on an arbitrary structure. The meaning of the matrix elements follows from the definition (1.5). Denoting complex amplitudes of both incident and reflected wave $E_{0_x} = E_{0_s}$ and $E_{0_y} = E_{0_p}$ we obtain

$$r_{ss} = \left(\frac{E_{0_s}^{(R)}}{E_{0_s}^{(I)}} \right)_{E_{0_p}^{(I)}=0}, \tag{1.7}$$

$$r_{sp} = \left(\frac{E_{0_s}^{(R)}}{E_{0_p}^{(I)}} \right)_{E_{0_s}^{(I)}=0}, \tag{1.8}$$

$$r_{ps} = \left(\frac{E_{0_p}^{(R)}}{E_{0_s}^{(I)}} \right)_{E_{0_p}^{(I)}=0}, \tag{1.9}$$

$$r_{pp} = \left(\frac{E_{0_p}^{(R)}}{E_{0_p}^{(I)}} \right)_{E_{0_s}^{(I)}=0}. \tag{1.10}$$

For description of transmission elements we use two Cartesian coordinate systems $\mathrm{S}^{(I)}$ and $\mathrm{S}^{(T)}$ according to the Fig. 1.3. The axes $x^{(I)}$, $x^{(T)}$ and $y^{(I)}$, $y^{(T)}$ are parallel, $z^{(I)}$ and $z^{(T)}$ are identical. Analogically to the previous case the polarization of the incident wave is in the system $\mathrm{S}^{(I)}$ characterized by a Jones

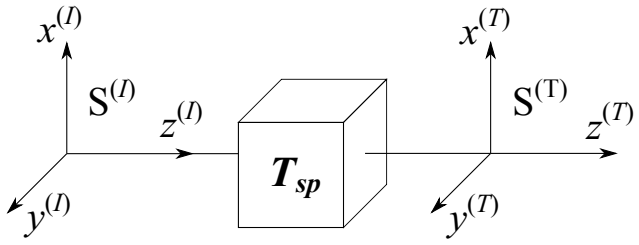

Figure 1.3: Transmission optical element with coordinate systems of the incident and transmitted wave.

vector $\boldsymbol{J}^{(I)}$. $\boldsymbol{J}^{(T)}$ describes the reflected light in the system $\mathrm{S}^{(T)}$ and their relation can be again written in a matrix form as

$$\boldsymbol{J}^{(T)} = \boldsymbol{T}_{sp} \cdot \boldsymbol{J}^{(I)}, \tag{1.11}$$

where $\boldsymbol{T}_{sp}$ stands for a Jones transmission matrix of a given optical element. We can express it as

$$\boldsymbol{T}_{sp} = \begin{bmatrix} t_{ss} & t_{sp} \\ t_{ps} & t_{pp} \end{bmatrix}. \tag{1.12}$$

Analogically, the meaning of the matrix components is given by (1.12) and we can write the relations

$$t_{ss} = \left(\frac{E_{0_s}^{(T)}}{E_{0_s}^{(I)}} \right)_{E_{0_p}^{(I)}=0}, \tag{1.13}$$

$$t_{sp} = \left(\frac{E_{0_s}^{(T)}}{E_{0_p}^{(I)}} \right)_{E_{0_s}^{(I)}=0}, \tag{1.14}$$

$$t_{ps} = \left(\frac{E_{0_p}^{(T)}}{E_{0_s}^{(I)}} \right)_{E_{0_p}^{(I)}=0}, \tag{1.15}$$

$$t_{pp} = \left(\frac{E_{0_p}^{(T)}}{E_{0_p}^{(I)}} \right)_{E_{0_s}^{(I)}=0}. \tag{1.16}$$

In case of an optical system consisting of N optical elements described by Jones matrices $\boldsymbol{X}_1, \boldsymbol{X}_2, \ldots, \boldsymbol{X}_N$, where $\boldsymbol{X}$ stands for either transmission or reflection matrix and we assume that the light passes through the elements in consecutive order $1, 2, \ldots, N$, the incident and final Jones vectors $\boldsymbol{J}^{(I)}$ and $\boldsymbol{J}^{(X)}$ are related as

$$\boldsymbol{J}^{(X)} = \boldsymbol{X}_N \cdot \boldsymbol{X}_{N-1} \cdots \boldsymbol{X}_1 \cdot \boldsymbol{J}^{(I)}. \tag{1.17}$$

1.3 Magneto-optical angles

We have already mentioned that when investigating the polarization we usually do not need to know neither the amplitude nor the absolute phase of the light wave. It is enough to know the two real parameters (θ, ϵ) or (α, δ). Therefore we introduce a quantity called complex polarization parameter χ which is given

by the ratio of the second and the first component of the Jones vector. With respect to (1.1) we can write

$$\chi = \frac{E_{0_y}}{E_{0_x}} = \tan\alpha e^{i\delta}. \tag{1.18}$$

Thus we obtain the parameters (α, δ) straightforwardly as

$$|\chi| = \tan\alpha, \tag{1.19}$$

$$\arg\chi = \delta. \tag{1.20}$$

If we take a Jones vector of an arbitrary elliptical polarization given by its azimuth θ and ellipticity angle ϵ expressed in Cartesian representation, we can write complex polarization parameter in the form [85]

$$\chi = \frac{\sin\theta\cos\epsilon + i\cos\theta\sin\epsilon}{\cos\theta\cos\epsilon - i\sin\theta\sin\epsilon} = \frac{\tan\theta + i\tan\epsilon}{1 - i\tan\theta\tan\epsilon}. \tag{1.21}$$

This can be further simplified assuming small angles θ and ϵ. Then we can approximate the tangents by their arguments, $\tan\theta \approx \theta$, $\tan\epsilon \approx \epsilon$. Neglecting also the second order term in denominator of (1.21) we obtain

$$\chi \approx \theta + i\epsilon. \tag{1.22}$$

In our experiment we usually use the Cartesian basis of s-polarized and p-polarized wave as was introduced before (see Fig. 1.2). Having an s-polarized incident wave in an isotropic medium (typically air) reflected upon an optically isotropic sample, the wave remains unchanged and after the reflection stays s-polarized due to the diagonality of the Jones reflection matrix. The same happens to a p-polarized wave. But in the case of an optically anisotropic sample (magnetized ferromagnetic layer), thus the Jones reflection matrix has non-zero off-diagonal components and one can observe a change of the polarization state when having an incident s or p-polarized wave.

Let us consider the case of s-polarized wave. Using (1.9) and (1.7) we can express a ratio of the off-diagonal r_{ps} to the diagonal r_{ss} component of the Jones reflection matrix,

$$\frac{r_{ps}}{r_{ss}} = \left(\frac{\frac{E_{0_p}^{(R)}}{E_{0_s}^{(I)}}}{\frac{E_{0_s}^{(R)}}{E_{0_s}^{(I)}}}\right)_{E_{0_p}^{(I)}=0} = \left(\frac{E_{0_p}^{(R)}}{E_{0_s}^{(R)}}\right)_{E_{0_p}^{(I)}=0} = \chi^{(R)}_{E_{0_p}^{(I)}=0} = \chi_s^{(R)}. \tag{1.23}$$

One can see that this ratio exactly corresponds with the definition (1.18) of the complex polarization parameter, therefore we denote it as a complex polarization parameter of the reflected wave $\chi_s^{(R)}$. In our case the parameters $\theta^{(R)}$ and $\epsilon^{(R)}$ of the reflected wave are small enough to allow us to use the approximation introduced above and write an analogy of (1.22)

$$\chi_s^{(R)} \approx \theta^{(R)} + i\epsilon^{(R)}. \tag{1.24}$$

Then we can finally define the complex Kerr magneto-optical angle Φ_{K_S} for incident s-polarized wave by a relation

$$\Phi_{K_S} \stackrel{\text{def}}{=} -\frac{r_{ps}}{r_{ss}} = -\chi_s^{(R)} \approx \theta_{K_S} - i\epsilon_{K_S}, \tag{1.25}$$

where θ_{K_S} and ϵ_{K_S} denote magneto-optical angles called Kerr rotation and Kerr ellipticity,

$$\theta_{K_S} \overset{\text{def}}{\approx} -\theta^{(R)}, \tag{1.26}$$

$$\epsilon_{K_S} \overset{\text{def}}{\approx} \epsilon^{(R)}. \tag{1.27}$$

In case of an incident p-polarized wave one can proceed in an analogical way. Using (1.8) and (1.10) we find out that the ratio of the off-diagonal r_{sp} to the diagonal r_{pp} matrix component equals to the inverse value of the complex polarization parameter of the reflected wave $\chi_p^{(R)}$. After calculating the complex polarization parameter in case of p-polarized incident wave [85] we can define complex Kerr MO angle

$$\Phi_{K_P} \overset{\text{def}}{=} \frac{r_{sp}}{r_{pp}} = \left(\chi_p^{(R)}\right)^{-1} \approx \theta_{K_P} - i\epsilon_{K_P}, \tag{1.28}$$

where Kerr rotation and Kerr ellipticity are given by

$$\theta_{K_P} \overset{\text{def}}{\approx} -\theta^{(R)} + \frac{\pi}{2}, \tag{1.29}$$

$$\epsilon_{K_P} \overset{\text{def}}{\approx} \epsilon^{(R)}. \tag{1.30}$$

In case of normal light incidence when having no plane of incidence and no distinction between s-polarized and p-polarized incident wave we obviously expect both definitions to become equal with the same resulting complex Kerr MO angles for both incident polarizations. It can be really shown [47] that in the case of normal light incidence the off-diagonal and diagonal Jones matrix components are respectively related

$$r_{ps} = r_{sp}, \qquad r_{pp} = -r_{ss}, \tag{1.31}$$

and therefore (1.25) and (1.28) are giving the same final expression of complex Kerr MO angle θ_K in case of normal light incidence,

$$\Phi_{K_S} = \Phi_{K_P} = \Phi_K = -\frac{r_{ps}}{r_{ss}} \approx \theta_K - i\epsilon_K. \tag{1.32}$$

One can do the same when investigating Faraday effect, after analogical assumptions and calculations one can define in a similar way the complex Faraday MO angle for both s and p-polarized incident waves using relations (1.13) - (1.16)

$$\Phi_{F_S} \overset{\text{def}}{=} \frac{t_{ps}}{t_{ss}} \approx \theta_{F_S} - i\epsilon_{F_S} \tag{1.33}$$

$$\Phi_{F_P} \overset{\text{def}}{=} -\frac{t_{sp}}{t_{pp}} \approx \theta_{F_P} - i\epsilon_{F_P}, \tag{1.34}$$

where θ_{F_S} and θ_{F_P} stand for Faraday rotation and the imaginary parts ϵ_{F_S} and ϵ_{F_P} are called magnetic circular dichroism (MCD). For our purposes we are interested mainly in Faraday effect at normal light incidence, therefore we can once again restrict ourselves to uniform expression where (1.33) and (1.34) become equal

$$\Phi_{F_S} = \Phi_{F_P} = \Phi_F = \frac{t_{ps}}{t_{ss}} \approx \theta_F - i\epsilon_F. \tag{1.35}$$

2. Theory of magneto-optical effects

2.1 Permittivity tensor

In previous chapter we have introduced the basics of description of the polarized light what allowed us to define the MO angles. Our next goal is to obtain the MO angles both theoretically and experimentally. In order to achieve that we start with the introduction of the permittivity tensor. Before we do so we introduce three basic geometries used for investigation of the magneto-optical Kerr effect (MOKE). The distinction is made according to the relative orientations of the plane of incidence, the surface of the sample and the magnetization vector $\boldsymbol{M}$ (see Fig. 2.1). In polar geometry the magnetization vector is perpendicular to the surface plane (it points against the direction of the z axis). In longitudinal geometry the magnetization vector lies in both, the plane of the interface and the plane of incidence (pointing along the y axis). Finally in transverse geometry the magnetization is in the plane of the interface, this time however it is perpendicular to the plane of incidence (pointing against the x axis). In our experiment we are interested in two of these geometries, polar and longitudinal one.

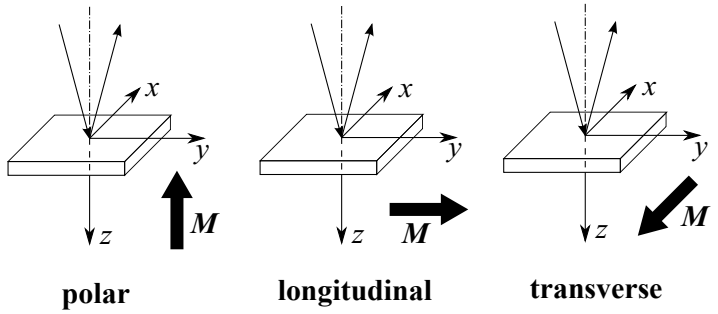

Figure 2.1: Three basic geometries of Kerr effect.

Material properties can be usually described either by permittivity, optical conductivity or susceptibility, which are all mutually related. In this thesis we use permittivity, which is in general a second-order tensor that can be expressed as

$$\varepsilon = \begin{bmatrix} \varepsilon_{xx} & \varepsilon_{xy} & \varepsilon_{xz} \\ \varepsilon_{yx} & \varepsilon_{yy} & \varepsilon_{yz} \\ \varepsilon_{zx} & \varepsilon_{zy} & \varepsilon_{zz} \end{bmatrix}. \tag{2.1}$$

Nevertheless this general form can be significantly simplified as will be shown.

Practice leads us to an assumption that the magnetization has only small influence on the permittivity tensor, thus we can expand its components into MacLaurin series

$$\varepsilon_{ij} = \varepsilon_{ij}(0) + \left(\frac{\partial \varepsilon_{ij}}{\partial M_k}\right)_{M=0} M_k + \left(\frac{\partial^2 \varepsilon_{ij}}{\partial M_k \partial M_l}\right)_{M=0} M_k M_l + \ldots \tag{2.2}$$

The first term of (2.2) $\varepsilon_{ij}(0)$ determines the tensor components when no external magnetic field is applied, the next terms are related to linear and quadratic MO

effects. In our case we deal with effects linearly proportional to magnetization, therefore in the series (2.2) we restrict ourselves to the first two terms. One can usually assume that the diagonal components are approximately equal and the off-diagonal ones are negligibly small compared to diagonal ones,

$$\varepsilon_{ii} \approx \varepsilon_{jj}, \qquad \varepsilon_{ij} \ll \varepsilon_{jj}, \qquad i,j = x,y,z \text{ and } i \neq j. \tag{2.3}$$

From symmetry arguments [47], which the permittivity tensor is supposed to satisfy in magnetic field, it can be shown that its general form (2.2) gets simplified. Considering also (2.3) and a specific geometry of the problem (see Fig. 2.1) we can rewrite the tensor in case of polar geometry as

$$\boldsymbol{\varepsilon_P} = \begin{bmatrix} \varepsilon_{xx} & \varepsilon_{xy} & 0 \\ -\varepsilon_{xy} & \varepsilon_{xx} & 0 \\ 0 & 0 & \varepsilon_{zz} \end{bmatrix} \approx \begin{bmatrix} \varepsilon_1 & -i\varepsilon_2 & 0 \\ i\varepsilon_2 & \varepsilon_1 & 0 \\ 0 & 0 & \varepsilon_1 \end{bmatrix} \tag{2.4}$$

and in case of longitudinal geometry as

$$\boldsymbol{\varepsilon_L} = \begin{bmatrix} \varepsilon_{xx} & 0 & -\varepsilon_{zx} \\ 0 & \varepsilon_{yy} & 0 \\ \varepsilon_{zx} & 0 & \varepsilon_{xx} \end{bmatrix} \approx \begin{bmatrix} \varepsilon_1 & 0 & -i\varepsilon_2 \\ 0 & \varepsilon_1 & 0 \\ i\varepsilon_2 & 0 & \varepsilon_1 \end{bmatrix}, \tag{2.5}$$

where we introduced a notation

$$\varepsilon_1 = \varepsilon_{xx} = \varepsilon_{yy} = \varepsilon_{zz}, \qquad i\varepsilon_2 = -\varepsilon_{xy} = \varepsilon_{zx}. \tag{2.6}$$

2.2 Microscopic theory

Since we have introduced the permittivity tensor in simplified form, we can start to calculate its components. In microscopic approach we begin with the Lorentz model describing an interaction of light wave with harmonically bounded electron with relaxation time τ. Let us assume the magnetic flux density of the external magnetic field pointing against the direction of the z axis, $\boldsymbol{B} = (0, 0, -B_z)$. As we have already mentioned in the previous chapter the electric component of light wave is dominating in the interaction with matter. Therefore we neglect the contribution of its magnetic field component. The equation of motion for the electron in a parabolic potential interacting with a wave propagating along the z axis of the Cartesian coordinate system is then given by a relation

$$m\frac{\partial^2 \boldsymbol{r}}{\partial t^2} + m\Gamma\frac{\partial \boldsymbol{r}}{\partial t} + m\omega_0^2 \boldsymbol{r} - e\frac{\partial \boldsymbol{r}}{\partial t} \times \boldsymbol{B} = eE_0 \mathrm{e}^{i\omega t}, \tag{2.7}$$

where m and e stand for the electron mass and elementary charge, $\boldsymbol{r}$ and ω_0 denote electron's position vector and its natural frequency, $\Gamma = \frac{1}{\tau}$ is a damping constant and $E_0\mathrm{e}^{i\omega t}$ is the electric component of the interacting wave. This equation can be decomposed into three components according to the Cartesian axes, consequently giving solution to all three components of the vector $\boldsymbol{r}$.

Considering the concentration of electrons N, the permittivity of vacuum ε_0, the susceptibility tensor $\boldsymbol{\chi}$ and the external electric field (of the light wave) $\boldsymbol{E}$ for the introduction of the average dipole moment per unit volume

$$\boldsymbol{P} = Ne\boldsymbol{r} = \varepsilon_0 \boldsymbol{\chi} \boldsymbol{E} = \varepsilon_0 (\boldsymbol{\varepsilon} - 1)\, \boldsymbol{E}, \tag{2.8}$$

we can obtain a relation between the components of the permittivity tensor and the solution of equation (2.7). From the symmetry of the problem it is natural to expect that the z component of the solution would be different from the x and y ones giving also different diagonal components of the permittivity tensor. That is truth, however we should realize that for our purposes we have simplified the tensor into the forms (2.4) and (2.5). Then using an assumption (2.6) we obtain all the diagonal permittivity tensor components resulting from the Lorentz model in an identical form [47]

$$\varepsilon_1 = 1 + \omega_p^2 \frac{1}{\omega_0^2 - \omega^2 + i\Gamma\omega}, \tag{2.9}$$

where $\omega_p = \frac{Ne^2}{m\varepsilon_0}$ denotes the plasma frequency. The off-diagonal components are given by [47]

$$\varepsilon_2 = -\omega_p^2 \frac{\omega_c \omega}{\left(\omega_0^2 - \omega^2 + i\Gamma\omega\right)^2 - \omega_c^2\omega^2}, \tag{2.10}$$

the frequency $\omega_c = -\frac{eB_z}{m}$ is the cyclotron frequency of a circular electron motion in a magnetic field.

Going deeper inside the microscopic approach, we continue with semiclassical theory of MO effects which considers the interaction of a classical electromagnetic wave with a quantum system. In this approach MO effects arise from splitting of the ground or exited energy levels of optical transitions. This is caused mainly by spin-orbit coupling and exchange interaction which enables the electrons to distinguish between two senses of circularly polarized light. In absence of spin-orbit coupling there is no contribution to off-diagonal permittivity tensor components ($\varepsilon_2 = 0$), therefore there is no MO effect. With respect to historical assumptions and considering the spin-orbit interaction we can distinguish between two particular cases of electron transitions.

In the first case we consider a transition from a singlet ground state to an excited state, which is split by spin-orbit interaction [38]

$$\Delta E = 2\hbar\Delta\omega_0 = 2\hbar\left(\omega_{0+} - \omega_{0-}\right), \tag{2.11}$$

where $\omega_{0\pm}$ are the distinct resonant frequencies for left and right circular polarizations. For this case one can derive [38] the behaviour of the off-diagonal element of the permittivity tensor. For our purposes we will use it in a form [75]

$$\varepsilon_2 = \Gamma_0^2(\varepsilon_2^{'})_{max} \frac{\left(\omega - \omega_0\right)^2 - \Gamma_0^2 + 2i\Gamma_0\left(\omega - \omega_0\right)}{\left[\left(\omega - \omega_0\right)^2 + \Gamma_0^2\right]^2}, \tag{2.12}$$

where ω_0 and Γ_0 are the resonant frequency and its half-width at half-maximum, $(\varepsilon_2^{'})_{max}$ denotes the maximum of the real part of the tensor component which occurs for $\omega = \omega_0$. Transitions of this type are called diamagnetic transitions. The real and imaginary parts of ε_2 are respectively even and odd functions of $\omega - \omega_0$. For $\Delta\omega_0 \ll \Gamma_0$ the real part has a simple dissipative line shape and the imaginary part shows a simple dispersive behaviour.

In the second case there is no splitting of both the ground and excited states, however spin-orbit interaction causes a difference between oscillator strengths f_+

and f_- for corresponding circular polarizations. The spectral dependence of the off-diagonal component can be analogically derived [38] in the form [75]

$$\varepsilon_2 = 2\Gamma_0(\varepsilon_2^{''})_{max}\frac{\omega\left(\omega^2-\omega_0^2+\Gamma_0^2\right)-i\Gamma_0\left(\omega^2+\omega_0^2-\Gamma_0^2\right)}{\left(\omega^2-\omega_0^2-\Gamma_0^2\right)^2+4\Gamma_0^2\omega^2}, \tag{2.13}$$

where $(\varepsilon_2^{''})_{max}$ is the maximum of the imaginary part which occurs for $\omega=\omega_0$. Such transitions are called paramagnetic transitions. The real and imaginary parts of the off-diagonal component are odd and even functions of $\omega-\omega_0$ and for $\Gamma_0 \ll \omega_0$ their spectral shapes are opposite compared to the previous case. The real part has a simple dispersive shape and the imaginary one shows a bell-shaped behaviour.

2.3 Macroscopic theory (Yeh's formalism)

So far we have defined MO effects via reflection and transmission coefficients and we have shown how to obtain components of the permittivity tensor from microscopic models. Now we will show the connection between these two topics and will introduce a way how to calculate the reflection and transmission coefficients from material parameters. For this purpose we use an approach developed by Yeh [84] and extended for absorbing media with magnetic ordering by Višňovský [78].

Let us take a look at a structure consisting of N layers (see Fig. 2.2). All interfaces are mutually parallel and at the same time perpendicular to the z axis. Surrounding half spaces 0 and $N+1$ are isotropic media characterized by permittivity scalars $\varepsilon^{(0)}$ and $\varepsilon^{(N+1)}$. Each layer of the investigated structure is described by complex permittivity tensor $\boldsymbol{\varepsilon}^{(n)}$ and thickness t_n for $n=1,2,\ldots,N$. The plane of incidence is perpendicular to the x axis, which makes the x component of the wave vector equal to zero and φ_0 denotes the angle of incidence.

In order to obtain the reflection coefficients, we first need to solve the wave equation in all layers of the investigated structure. Let us consider monochromatic plane wave of a defined polarization, which impacts on a magnetized ferromagnetic (therefore anisotropic) medium without free charges from vacuum (or air). The electromagnetic wave in such medium can be described using Maxwell and constitutive equations. The relative permittivity and permeability are in general second-order tensors, however for our purposes it will be precise enough to consider the relative permeability equal to one [51] while we keep the permittivity tensor in its general form (2.1). One can then simply derive the wave equation for the electric component of the wave in the n-th layer in its well known form

$$\Delta\boldsymbol{E}^{(n)} - \frac{\boldsymbol{\varepsilon}^{(n)}}{c^2}\frac{\partial^2\boldsymbol{E}^{(n)}}{\partial t^2} - \nabla\left(\nabla\cdot\boldsymbol{E}^{(n)}\right) = 0, \tag{2.14}$$

where c stands for the speed of light in vacuum. We consider the solution in the form of plane wave with frequency ω and wave vector $\boldsymbol{k}^{(n)}$. Using this solution we can rewrite the equation (2.14) in a matrix form [85]

$$\begin{bmatrix} \varepsilon_{xx}^{(n)}-N_y^2-N_z^{(n)^2} & \varepsilon_{xy}^{(n)} & \varepsilon_{xz}^{(n)} \\ \varepsilon_{yx}^{(n)} & \varepsilon_{yy}^{(n)}-N_z^{(n)^2} & \varepsilon_{yz}^{(n)}+N_yN_z^{(n)} \\ \varepsilon_{zx}^{(n)} & \varepsilon_{zy}^{(n)}+N_yN_z^{(n)} & \varepsilon_{zz}^{(n)}-N_y^2 \end{bmatrix} \begin{bmatrix} E_{0x}^{(n)} \\ E_{0y}^{(n)} \\ E_{0z}^{(n)} \end{bmatrix} = 0, \tag{2.15}$$

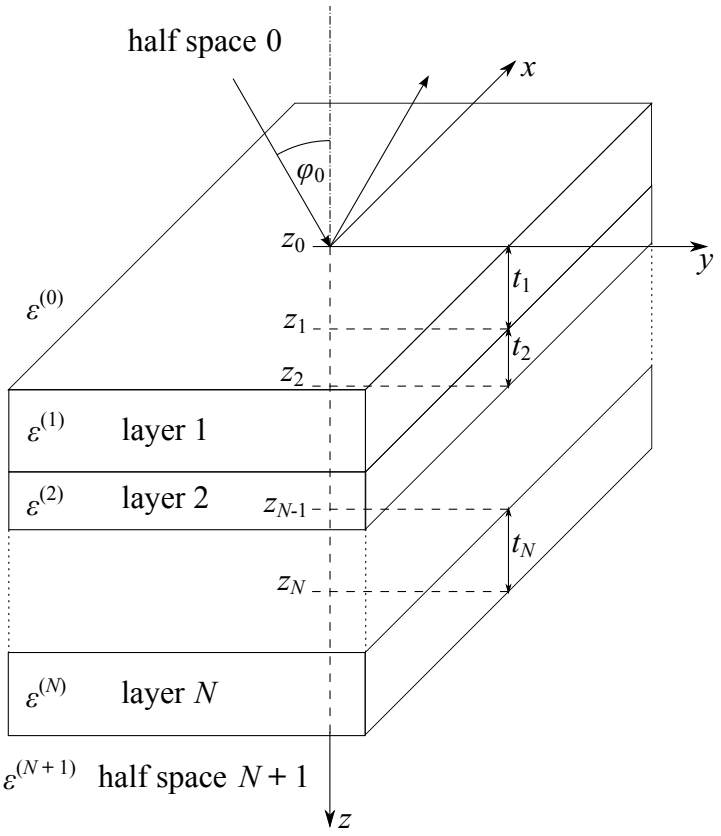

Figure 2.2: Multilayer structure surrounded by two isotropic half spaces.

where $E_{0x}^{(n)}$, $E_{0y}^{(n)}$ and $E_{0z}^{(n)}$ denote the components of the complex amplitude of the wave and N_y, $N_z^{(n)}$ are components of the reduced wave vector which is given by

$$\boldsymbol{N}^{(n)} = \frac{c}{\omega}\boldsymbol{k}^{(n)} = \left(N_x x + N_y y + N_z^{(n)} z\right). \tag{2.16}$$

With respect to choice of Cartesian system, its x component is zero throughout the structure and y component is the same in all layers due to Snell law

$$N_y = N_0 \sin\varphi_0, \tag{2.17}$$

where N_0 is the real refractive index of the isotropic front medium. The non-trivial solution of equation (2.15) requires a condition for zero determinant, which leads us to a characteristic equation for four eigenvalues $N_{z_j}^{(n)}$. These solutions describe the eigenmodes of the light waves for a given anisotropic material. The modes are given by four eigenvectors $\boldsymbol{e}_j^{(n)}$ corresponding to the four solutions of the characteristic equation. The general solution of (2.15) is then given by linear combination of these four eigenmodes

$$\boldsymbol{E}^{(n)} = \sum_{j=1}^{4} E_{0_j}^{(n)}(z_n)\,\boldsymbol{e}_j^{(n)} e^{i\left\{\omega t - \frac{\omega}{c}\left[N_y y + N_{z_j}^{(n)}(z-z_n)\right]\right\}}, \tag{2.18}$$

where z_n denotes the z component of the interface between n-th and n+first layer. The relation between electric and magnetic field component of the wave follows from Maxwell equations

$$\boldsymbol{B}^{(n)} = \frac{1}{c}\boldsymbol{N}^{(n)} \times \boldsymbol{E}^{(n)}. \tag{2.19}$$

Therefore we can write for the magnetic component

$$\boldsymbol{B}^{(n)} = \frac{1}{c}\sum_{j=1}^{4} E_{0_j}^{(n)}\left(z_n\right)\boldsymbol{b}_j^{(n)} e^{i\left\{\omega t - \frac{\omega}{c}\left[N_y y + N_{z_j}^{(n)}(z-z_n)\right]\right\}}, \tag{2.20}$$

where the eigenvectors $\boldsymbol{b}_j^{(n)}$ are according to (2.19) given by

$$\boldsymbol{b}_j^{(n)} = \boldsymbol{N}^{(n)} \times \boldsymbol{e}_j^{(n)}. \tag{2.21}$$

Having the solution of the wave equation we can now proceed to the next step which is a consideration of the boundary conditions. It can be shown from Maxwell equations that the tangential components of the electric and magnetic field vectors are continuous at the interface between two media. This can be, with respect to (2.18) and (2.20), expressed in case of $n-1$st and n-th layer as [85]

$$\sum_{j=1}^{4} E_{0_j}^{(n-1)}\left(z_{n-1}\right)\boldsymbol{e}_j^{(n-1)}\cdot\boldsymbol{x} = \sum_{j=1}^{4} E_{0_j}^{(n)}\left(z_n\right)\boldsymbol{e}_j^{(n)}\cdot\boldsymbol{x} e^{i\frac{\omega}{c}N_{z_j}^{(n)}t_n}, \tag{2.22}$$

$$\sum_{j=1}^{4} E_{0_j}^{(n-1)}\left(z_{n-1}\right)\boldsymbol{b}_j^{(n-1)}\cdot\boldsymbol{y} = \sum_{j=1}^{4} E_{0_j}^{(n)}\left(z_n\right)\boldsymbol{b}_j^{(n)}\cdot\boldsymbol{y} e^{i\frac{\omega}{c}N_{z_j}^{(n)}t_n}, \tag{2.23}$$

$$\sum_{j=1}^{4} E_{0_j}^{(n-1)}\left(z_{n-1}\right)\boldsymbol{e}_j^{(n-1)}\cdot\boldsymbol{y} = \sum_{j=1}^{4} E_{0_j}^{(n)}\left(z_n\right)\boldsymbol{e}_j^{(n)}\cdot\boldsymbol{y} e^{i\frac{\omega}{c}N_{z_j}^{(n)}t_n}, \tag{2.24}$$

$$\sum_{j=1}^{4} E_{0_j}^{(n-1)}\left(z_{n-1}\right)\boldsymbol{b}_j^{(n-1)}\cdot\boldsymbol{x} = \sum_{j=1}^{4} E_{0_j}^{(n)}\left(z_n\right)\boldsymbol{b}_j^{(n)}\cdot\boldsymbol{x} e^{i\frac{\omega}{c}N_{z_j}^{(n)}t_n}, \tag{2.25}$$

and it can be rewritten in a matrix form

$$\boldsymbol{D}^{(n-1)}\boldsymbol{E}_0^{(n-1)}\left(z_{n-1}\right) = \boldsymbol{D}^{(n)}\boldsymbol{P}^{(n)}\boldsymbol{E}_0^{(n)}\left(z_n\right). \tag{2.26}$$

Here $\boldsymbol{D}^{(n)}$ is called the dynamical matrix of the n-th layer and $\boldsymbol{P}^{(n)}$ stands for the so-called propagation matrix. The dynamical matrix characterizes the transformation of the wave at the interface and consists of the x and y components of the eigenmodes

$$\boldsymbol{D}^{(n)} = \begin{bmatrix} \boldsymbol{e}_1^{(n)}\cdot\boldsymbol{x} & \boldsymbol{e}_2^{(n)}\cdot\boldsymbol{x} & \boldsymbol{e}_3^{(n)}\cdot\boldsymbol{x} & \boldsymbol{e}_4^{(n)}\cdot\boldsymbol{x} \\ \boldsymbol{b}_1^{(n)}\cdot\boldsymbol{y} & \boldsymbol{b}_2^{(n)}\cdot\boldsymbol{y} & \boldsymbol{b}_3^{(n)}\cdot\boldsymbol{y} & \boldsymbol{b}_4^{(n)}\cdot\boldsymbol{y} \\ \boldsymbol{e}_1^{(n)}\cdot\boldsymbol{y} & \boldsymbol{e}_2^{(n)}\cdot\boldsymbol{y} & \boldsymbol{e}_3^{(n)}\cdot\boldsymbol{y} & \boldsymbol{e}_4^{(n)}\cdot\boldsymbol{y} \\ \boldsymbol{b}_1^{(n)}\cdot\boldsymbol{x} & \boldsymbol{b}_2^{(n)}\cdot\boldsymbol{x} & \boldsymbol{b}_3^{(n)}\cdot\boldsymbol{x} & \boldsymbol{b}_4^{(n)}\cdot\boldsymbol{x} \end{bmatrix}. \tag{2.27}$$

The propagation matrix describes the propagation of the wave in the n-th layer and with respect to (2.22) - (2.25) we can write it as

$$\boldsymbol{P}^{(n)} = \begin{bmatrix} e^{i\frac{\omega}{c}N_{z_1}^{(n)}t_n} & 0 & 0 & 0 \\ 0 & e^{i\frac{\omega}{c}N_{z_2}^{(n)}t_n} & 0 & 0 \\ 0 & 0 & e^{i\frac{\omega}{c}N_{z_3}^{(n)}t_n} & 0 \\ 0 & 0 & 0 & e^{i\frac{\omega}{c}N_{z_4}^{(n)}t_n} \end{bmatrix}. \tag{2.28}$$

Now we can further rewrite the continuity requirements (2.26) in a form

$$\boldsymbol{E}_0^{(n-1)}\left(z_{n-1}\right) = \left(\boldsymbol{D}^{(n-1)}\right)^{-1} \boldsymbol{D}^{(n)} \boldsymbol{P}^{(n)} \boldsymbol{E}_0^{(n)}\left(z_n\right) = \boldsymbol{T}^{(n-1,n)} \boldsymbol{E}_0^{(n)}\left(z_n\right), \tag{2.29}$$

where we have introduced a transfer matrix $\boldsymbol{T}^{(n-1,n)}$ which binds the field components in the two adjacent layers. The field components are related in this way at all the interfaces, therefore we can successively multiply all the transfer matrices and express the relation between the waves in surrounding media as

$$\boldsymbol{E}_0^{(0)}\left(z_0\right) = \left(\prod_{n=1}^{N+1} \boldsymbol{T}^{(n-1,n)}\right) \boldsymbol{E}_0^{(N+1)}\left(z_N\right) = \boldsymbol{M}\boldsymbol{E}_0^{(N+1)}\left(z_N\right). \tag{2.30}$$

Here we introduced the matrix $\boldsymbol{M}$ which characterizes an arbitrary anisotropic multilayer structure. Considering now that the incident wave can be in the front half space decomposed into two orthogonal polarizations $\boldsymbol{e}_1^{(0)}$ and $\boldsymbol{e}_3^{(0)}$ having amplitudes $E_{01}^{(0)}$ and $E_{03}^{(0)}$ and taking into account that there is no source of light in the back half space (therefore $E_{02}^{(n+1)} = E_{04}^{(n+1)} = 0$), we rewrite equation (2.30) in a form

$$\begin{bmatrix} E_{01}^{(0)} \\ E_{02}^{(0)} \\ E_{03}^{(0)} \\ E_{04}^{(0)} \end{bmatrix} = \begin{bmatrix} M_{11} & M_{12} & M_{13} & M_{14} \\ M_{21} & M_{22} & M_{23} & M_{24} \\ M_{31} & M_{32} & M_{33} & M_{34} \\ M_{41} & M_{42} & M_{43} & M_{44} \end{bmatrix} \begin{bmatrix} E_{01}^{(N+1)} \\ 0 \\ E_{03}^{(N+1)} \\ 0 \end{bmatrix}. \tag{2.31}$$

Finally from this set of equations one can calculate the reflection coefficients in terms of the components of the matrix $\boldsymbol{M}$ [79]

$$r_{21} = \left(\frac{E_{02}^{(0)}}{E_{01}^{(0)}}\right)_{E_{03}^{(0)}=0} = \frac{M_{21}M_{33} - M_{23}M_{31}}{M_{11}M_{33} - M_{13}M_{31}}, \tag{2.32}$$

$$r_{23} = \left(\frac{E_{02}^{(0)}}{E_{03}^{(0)}}\right)_{E_{01}^{(0)}=0} = \frac{M_{11}M_{23} - M_{21}M_{13}}{M_{11}M_{33} - M_{13}M_{31}}, \tag{2.33}$$

$$r_{41} = \left(\frac{E_{04}^{(0)}}{E_{01}^{(0)}}\right)_{E_{03}^{(0)}=0} = \frac{M_{41}M_{33} - M_{43}M_{31}}{M_{11}M_{33} - M_{13}M_{31}}, \tag{2.34}$$

$$r_{43} = \left(\frac{E_{04}^{(0)}}{E_{03}^{(0)}}\right)_{E_{01}^{(0)}=0} = \frac{M_{11}M_{43} - M_{41}M_{13}}{M_{11}M_{33} - M_{13}M_{31}}. \tag{2.35}$$

If we assume the decomposition of the incident and reflected wave into s-polarized and p-polarized component then the reflection coefficients (2.32) - (2.35) are related to the elements of the Jones reflection matrix (1.6) as follows

$$\boldsymbol{R}_{sp} = \begin{bmatrix} r_{ss} & r_{sp} \\ r_{ps} & r_{pp} \end{bmatrix} = \begin{bmatrix} r_{21} & r_{32} \\ -r_{41} & -r_{43} \end{bmatrix}. \tag{2.36}$$

In case of transmission coefficients one can do the same and get the relations

in the form [79]

$$t_{11} = \left(\frac{E_{01}^{(N+1)}}{E_{01}^{(0)}} \right)_{E_{03}^{(0)}=0} = \frac{M_{33}}{M_{11}M_{33} - M_{13}M_{31}}, \tag{2.37}$$

$$t_{13} = \left(\frac{E_{01}^{(N+1)}}{E_{03}^{(0)}} \right)_{E_{01}^{(0)}=0} = \frac{-M_{13}}{M_{11}M_{33} - M_{13}M_{31}}, \tag{2.38}$$

$$t_{31} = \left(\frac{E_{03}^{(N+1)}}{E_{01}^{(0)}} \right)_{E_{03}^{(0)}=0} = \frac{-M_{31}}{M_{11}M_{33} - M_{13}M_{31}}, \tag{2.39}$$

$$t_{33} = \left(\frac{E_{03}^{(N+1)}}{E_{03}^{(0)}} \right)_{E_{01}^{(0)}=0} = \frac{M_{11}}{M_{11}M_{33} - M_{13}M_{31}}. \tag{2.40}$$

These transmission coefficients are analogically related to the components of the Jones transmission matrix (1.12)

$$\boldsymbol{T}_{sp} = \begin{bmatrix} t_{ss} & t_{sp} \\ t_{ps} & t_{pp} \end{bmatrix} = \begin{bmatrix} t_{11} & t_{13} \\ t_{31} & t_{33} \end{bmatrix}. \tag{2.41}$$

Thus now thanks to the relations (2.32) - (2.35) and (2.37) - (2.40) we can, from material parameters given by the elements of the permittivity tensor and from known thicknesses of the layers, express the MO effects according to their definitions (1.25), (1.28) and (1.33), (1.34). We can do so for an arbitrary anisotropic multilayer structure.

3. Experimental techniques

In previous chapters we have introduced the theoretical background necessary for dealing with MO phenomena and we have shown how to obtain MO angles in a pure theoretical way. So now we can start to talk about the experimental approach. Before we describe the set-up used for MO measurements let us mention few words about the preparation of the samples.

3.1 Pulsed laser deposition

The first attempts to use laser for fabrication of thin films had been performed already soon after its discovery in the 1960s [64, 22]. However the quality of prepared films used to be inferior compared to other conventional methods, e.g. molecular beam epitaxy (MBE) or metalorganic chemical vapour deposition (MOCVD). The situation had begun to change in the late 1980s thanks to the success in the use of pulsed laser deposition (PLD) in order to grow high quality superconducting Y-Ba-Cu-O thin films [13, 27]. Since these days PLD has become a widely spread method used for fabrication of thin layers of various materials including insulators, semiconductors, metals, polymers and even biological materials [14].

The typical experimental set-up for PLD is shown in Fig. 3.1. A dense ceramic target of the desired material together with a substrate are placed in a vacuum chamber. A short ($\sim$ ns) and high-energy ($\sim$ J/cm^2) laser pulse impacts

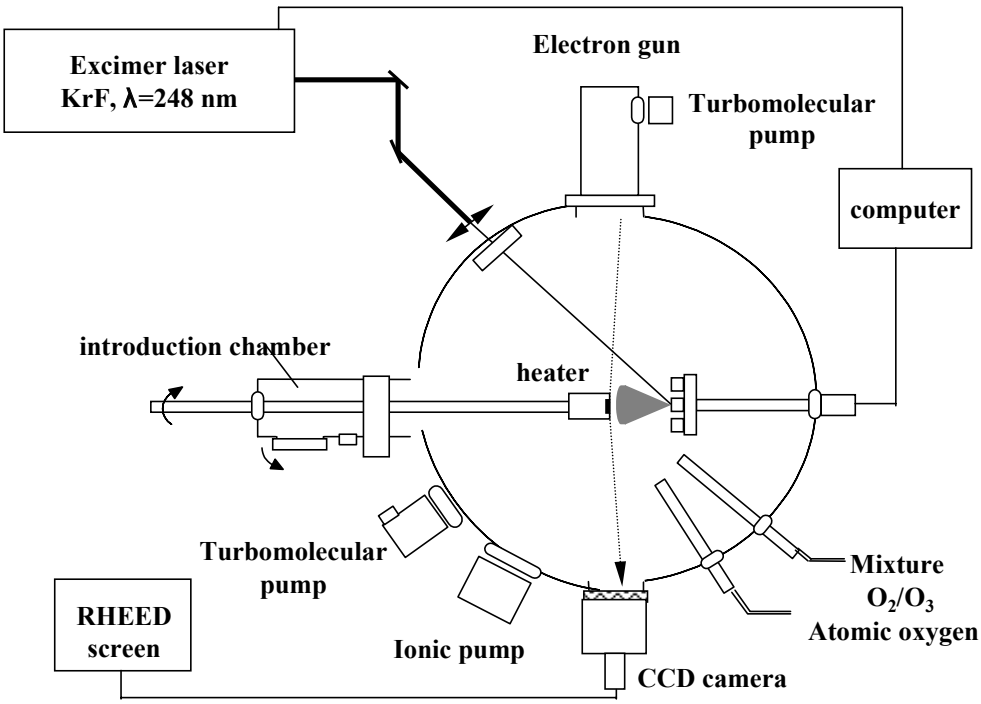

Figure 3.1: Typical PLD experimental set-up for fabrication of magnetic oxides [54].

on the target, evaporates a small amount of the material creating a plasma plume.

After few microseconds the plume hits the substrate which is maintained at high temperature (typically hundreds of degrees Celsius) and condenses while growing the desired film. Analogically to MBE set-ups, the proper epitaxial growth of the layers can be monitored by reflection high-energy electron diffraction (RHEED).

To achieve epitaxial growth, PLD has proven itself to be remarkably efficient when fabricating multicomponent inorganic materials [14]. It can be realized when the ablation plume consists mostly of atomic, diatomic and other low-mass components. Therefore we need to use ultraviolet (UV) wavelength of the laser and nanosecond pulses to cause a strong absorption in a small volume of the target material. For other materials as polymers or organic materials different conditions are applied.

Besides the capability of epitaxial growth there are several other characteristics making PLD of high interest for growth of thin films, e.g. stoichiometric transfer of material between target and substrate, generation of energetic molecules and compatibility with background pressures from ultrahigh vacuum ($\sim 10^{-7}$ Pa) up to circa 10^2 Pa. However it is still necessary to have at least medium vacuum in contrast to MOCVD, which is working at almost atmospheric pressure.

The presence of a background gas serves two purposes. In our case when growing oxides the oxygen atmosphere helps to provide proper stoichiometry of the fabricated films. The second reason is a relatively high energy of the ablated species. Dynamics studies of the plasma plume have shown that energies of several hundred electron volts [10] are reachable. But molecules which are hitting the film with energy from ~ 50 eV could damage its structure. The background gas is able to decrease the energy of evaporated species down bellow 1 eV and therefore prevent the undesirable violation of the growth process.

One last remark belongs to oxygen annealing which usually leads to essential improvements of the physical properties as T_C or CMR [54]. According to a particular deposition process the oxygen annealing can either help to additionally oxidize the grown film or in contrary to remove extra oxygen. Both ways lead to final optimization.

3.2 Spectroscopic ellipsometry

Prior to the introduction of MO spectroscopy let us talk briefly about a technique which is also important for data analysis of MO experiments. Its importance originates in providing information about optical properties of investigated materials, i.e. it provides the knowledge of the complex index of refraction, which is directly related to the diagonal component of the permittivity tensor.

The basic set-up of a spectroscopic ellipsometer is shown in Fig. 3.2. Light coming out of the source passes through the polarizer P which determines linear polarization of the light wave. The plane of polarization is given by an angle α measured with respect to the x axis which is perpendicular to the wave vector and also to the plane of incidence. In terms of Jones calculus we can express the Jones transmission matrix of the polariser as

$$\boldsymbol{T}_P = \begin{bmatrix} \cos^2\alpha & \cos\alpha\sin\alpha \\ \cos\alpha\sin\alpha & \sin^2\alpha \end{bmatrix}. \tag{3.1}$$

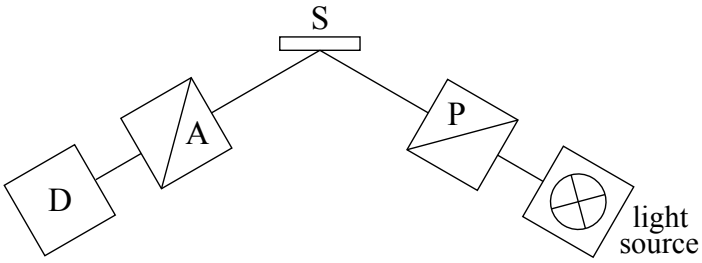

Figure 3.2: Basic experimental set-up for ellipsometry measurements; A - analyzer, D - detector, P - polarizer, S - sample.

Then the light reflects on the investigated sample S. In first chapter we have introduced the Jones reflection matrix in its general form (1.6), however in the case of ellipsometry we deal with isotropic materials (for MO measurements we gain the anisotropy by placing the sample in a magnetic field), therefore the Jones reflection matrix (1.6) has a simplified diagonal form

$$\boldsymbol{R}_{sp} = \begin{bmatrix} r_s & 0 \\ 0 & r_p \end{bmatrix}. \tag{3.2}$$

The reflected wave passes through an analyzer which is a polarizer transmitting linearly polarized light given by an angle ξ measured to the x axis. Thus analogically to (3.1) we can write its Jones matrix

$$\boldsymbol{T}_A = \begin{bmatrix} \cos^2\xi & \cos\xi\sin\xi \\ \cos\xi\sin\xi & \sin^2\xi \end{bmatrix}. \tag{3.3}$$

Relation between the incident $\boldsymbol{J}^{(I)}$ and final $\boldsymbol{J}^{(X)}$ Jones vectors is then, with respect to (3.1) - (3.3), given by (1.17) which determines the polarization state of light passed through an arbitrary optical system,

$$\begin{aligned} \boldsymbol{J}^{(X)} &= \boldsymbol{T}_A \cdot \boldsymbol{R}_{sp} \cdot \boldsymbol{T}_P \cdot \boldsymbol{J}^{(I)} = \\ &= \begin{bmatrix} \cos^2\xi & \cos\xi\sin\xi \\ \cos\xi\sin\xi & \sin^2\xi \end{bmatrix} \begin{bmatrix} r_s & 0 \\ 0 & r_p \end{bmatrix} \begin{bmatrix} \cos^2\alpha & \cos\alpha\sin\alpha \\ \cos\alpha\sin\alpha & \sin^2\alpha \end{bmatrix} \boldsymbol{J}^{(I)}. \end{aligned} \tag{3.4}$$

In ellipsometry we are interested in a change of s and p-polarized component upon reflection in their relation to each other. It can be expressed by complex reflectance ratio

$$\rho = \frac{r_p}{r_s} = \tan\Psi e^{i\Delta} \tag{3.5}$$

which uses the elements of the simplified Jones reflection matrix (3.2) and which introduces the ellipsometric angles Ψ and Δ. The intensity I arriving at the detector D is given by the final state of the Jones vector from (3.4)

$$I = \left(\boldsymbol{J}^{(X)}\right)^{\dagger} \boldsymbol{J}^{(X)}. \tag{3.6}$$

The detected intensity contains overall information from which the ellipsometric angles Ψ and Δ can be extracted. We can calculate the physical properties of the investigated sample such as the film thickness and optical parameters - index of refraction n and extinction coefficient k. In order to do so, we typically need

to consider model structure of the investigated material and numerically adjust the desired parameters by repeated comparison with the experimental data. Since we are interested in the permittivity tensor, it would be useful to write the well known relation between its diagonal component $\varepsilon_1 = \varepsilon_1^{'} + i\varepsilon_1^{''}$ and the complex index of refraction $\tilde{n} = n + ik$,

$$\varepsilon_1 = (\tilde{n})^2 . \tag{3.7}$$

This relation eventually helps us to calculate the desired component of the permittivity tensor from the measured experimental parameters Ψ and Δ when considering proper model structure of the sample.

The experimental set-up presented in this section and depicted in Fig. 3.2 serves only as an introduction of the basic idea of ellipsometry. We assume completely polarized light satisfying the needs of Jones calculus. However the real situation is usually different, the typical experimental set-up therefore involves also phase retarder which allows us to measure how much of light becomes unpolarized. Depolarization occurs for example due to non-uniformity of the sample or as a result of backside reflection at the interface of the investigated film and its substrate layer. Therefore its knowledge could be helpful in the characterization process.

3.3 Magneto-optical spectroscopy

Let us now take a look at the experimental technique essential for the purposes of this work. We can describe the basic principle of MO spectroscopy by simply saying that it is a spectroscopic ellipsometry performed in a magnetic field. Therefore it is sometimes referred as magneto-optical spectroscopic ellipsometry [79]. Why it is so we can easily understand taking look at the MOKE spectrometer in Fig. 3.3 and recognizing some features characteristic for ellipsometry measurements. The essence of the apparatus is once again the work with polarized light using the polarizer P and analyzer A. The main difference lies in the magnetic field applied to the investigated sample, which becomes optically anisotropic, having non-zero also off-diagonal components of its Jones reflection matrix (1.6). Thus providing information necessary to obtain the MO angles according to their definitions in the first chapter. There have been invented several methods for measuring the components of the Jones reflection matrix. The simplest of them perform direct intensity detection, the more complicated ones with higher signal to noise ratio are based on the modulation of azimuth or ellipticity of the incident wave. More detailed overview of both groups of techniques can be find for example in [47] or [75]. Here we focus only on the one method employed in our experiment, which is the azimuth modulation technique.

The simplified diagram of MOKE spectrometer is depicted in Fig. 3.3. High pressure Xe lamp is employed as a light source, allowing us to perform the measurements in a spectral range from 1.2 eV to 5,6 eV. Then the light passes through the prism monochromator SPM-2. Since the linear polarization is defined analogically to the previous case by polariser P in a plane given by the angle α, we can write the Jones matrix of the polariser P as in equation (3.1). Afterwards the light is passing through two optical elements which are utilizing Faraday effect in quartz. They are both made of a fused quartz rod with optically polished

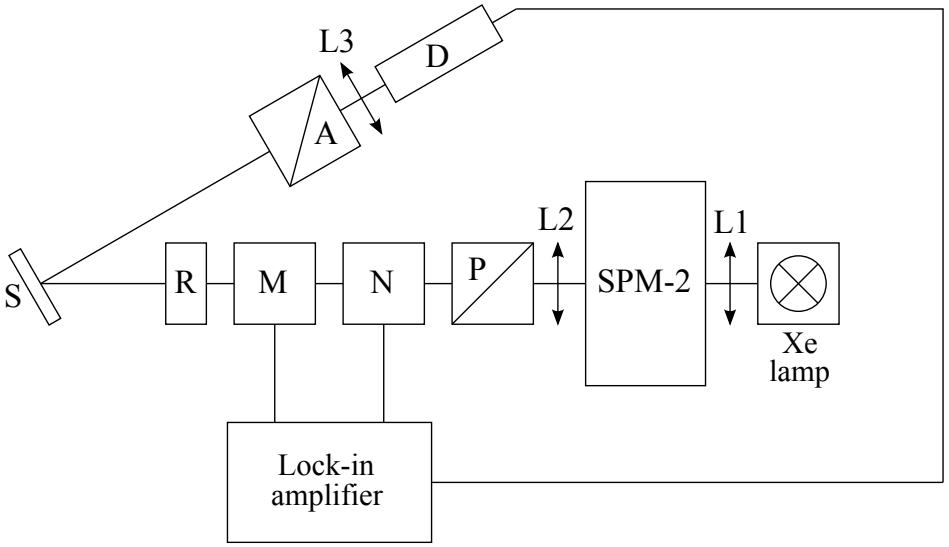

Figure 3.3: Simplified diagram of spectrometer for MO Kerr effect measurements; A - analyzer, D - detector, L1, L2, L3 - lenses, M - Faraday modulation cell, N - Faraday null cell, P - polariser, R - phase retarder, S - sample.

faces, inserted into a solenoid coil. First is Faraday null cell N which changes the azimuth of the light by value η proportional to a current controlled by a feedback loop. Its Jones transmission matrix can be written in a form

$$\boldsymbol{T}_N = \begin{bmatrix} \cos\eta & -\sin\eta \\ \sin\eta & \cos\eta \end{bmatrix}. \tag{3.8}$$

The Faraday modulation cell M is controlled by reference signal of the Lock-in amplifier which is modulating the azimuth of the light wave by an angle $\beta = \beta_0 \sin\omega t$, where β_0 stands for the amplitude of the modulation angle and ω is the modulation frequency. The Jones matrix of the modulation cell can be then written as

$$\boldsymbol{T}_M = \begin{bmatrix} \cos\beta & -\sin\beta \\ \sin\beta & \cos\beta \end{bmatrix} = \begin{bmatrix} \cos(\beta_0 \sin\omega t) & -\sin(\beta_0 \sin\omega t) \\ \sin(\beta_0 \sin\omega t) & \cos(\beta_0 \sin\omega t) \end{bmatrix}. \tag{3.9}$$

Another component of the system is a phase retarder R characterized by its phase shift δ. One can write its transmission matrix in a form

$$\boldsymbol{T}_R = \begin{bmatrix} e^{i\frac{\delta}{2}} & 0 \\ 0 & e^{-i\frac{\delta}{2}} \end{bmatrix}. \tag{3.10}$$

The reflection upon the sample S is characterized by Jones reflection matrix (1.5), which is now due to anisotropy having its general form. After reflection the light passes through the analyzer A which transmits a given linear polarization.

Having matrix expressions of all the components of the spectrometer we can write the relation between the initial $\boldsymbol{J}^{(I)}$ and final $\boldsymbol{J}^{(X)}$ polarization state of the

wave according to (1.17) as

$$\boldsymbol{J}^{(X)} = \boldsymbol{T}_A \cdot \boldsymbol{R}_{sp} \cdot \boldsymbol{T}_R \cdot \boldsymbol{T}_M \cdot \boldsymbol{T}_N \cdot \boldsymbol{T}_P \cdot \boldsymbol{J}^{(I)} = \begin{bmatrix} \cos^2\xi & \cos\xi\sin\xi \\ \cos\xi\sin\xi & \sin^2\xi \end{bmatrix} \cdot$$
$$\cdot \begin{bmatrix} r_{ss} & r_{sp} \\ r_{ps} & r_{pp} \end{bmatrix} \cdot \begin{bmatrix} e^{i\frac{\delta}{2}} & 0 \\ 0 & e^{-i\frac{\delta}{2}} \end{bmatrix} \cdot \begin{bmatrix} \cos(\beta_0 \sin\omega t) & -\sin(\beta_0 \sin\omega t) \\ \sin(\beta_0 \sin\omega t) & \cos(\beta_0 \sin\omega t) \end{bmatrix} \cdot \quad (3.11)$$
$$\cdot \begin{bmatrix} \cos\eta & -\sin\eta \\ \sin\eta & \cos\eta \end{bmatrix} \cdot \begin{bmatrix} \cos^2\alpha & \cos\alpha\sin\alpha \\ \cos\alpha\sin\alpha & \sin^2\alpha \end{bmatrix} \cdot \boldsymbol{J}^{(I)}.$$

If we consider that in our experiment we work with either s or p-polarized wave passing through the analyzer, which makes the angle ξ equal to either 0 or $\frac{\pi}{2}$, the final state of the Jones vector (3.11) can be written in the form

$$\boldsymbol{J}^{(X)} = \begin{bmatrix} \cos^2\xi(r_{ss}e^{i\frac{\delta}{2}}\cos\Omega + r_{sp}e^{-i\frac{\delta}{2}}\sin\Omega) \\ \sin^2\xi(r_{ps}e^{i\frac{\delta}{2}}\cos\Omega + r_{pp}e^{-i\frac{\delta}{2}}\sin\Omega) \end{bmatrix}, \quad \Omega = \alpha + \eta + \beta_0 \sin\omega t. \quad (3.12)$$

The intensity of light arriving at the detector D is then given by a relation analogical to (3.6). We use a photomultiplier as a detector, which roughly covers the spectral range of the used Xe lamp. Detected signal is brought to the lock-in amplifier. Oscillating component at the modulation frequency is directly proportional to an angle Γ, which represents the contribution of the MO effect. Via this quantity the output voltage from the lock-in amplifier is controlled, this voltage determines the angle η of the Faraday null cell which is compensating the MO effect in the investigated sample. This is the way how the feedback loop controls the experiment. If we take a more detailed look at the description of the feedback loop [47, 75] it can be derived how the angle Γ is related to the phase shift δ of the phase retarder and to the MO angles. For incident s and p-polarized wave we obtain in case of the polar geometry

$$\Gamma_s(\delta) \approx -\mathrm{Re}\{\Phi_{K_S}e^{-i\delta}\} \approx -\theta_{K_S}\cos\delta + \epsilon_{K_S}\sin\delta, \quad (3.13)$$
$$\Gamma_p(\delta) \approx -\mathrm{Re}\{\Phi_{K_P}e^{i\delta}\} \approx -\theta_{K_P}\cos\delta - \epsilon_{K_P}\sin\delta \quad (3.14)$$

and in case of the longitudinal geometry

$$\Gamma_s(\delta) \approx \mathrm{Re}\{\Phi_{K_S}e^{-i\delta}\} \approx \theta_{K_S}\cos\delta - \epsilon_{K_S}\sin\delta, \quad (3.15)$$
$$\Gamma_p(\delta) \approx \mathrm{Re}\{\Phi_{K_P}e^{i\delta}\} \approx \theta_{K_P}\cos\delta + \epsilon_{K_P}\sin\delta. \quad (3.16)$$

During the experiment we measure the current flowing through the compensation cell, which is proportional to the angle Γ. From (3.13) - (3.16) we can see that with no phase retarder in our apparatus ($\delta = 0$) we measure directly the spectrum of Kerr rotation. We could theoretically obtain directly also the spectrum of Kerr ellipticity when using phase retarder with the phase shift $\delta = \frac{\pi}{2}$. However no real phase retarder have a constant phase shift in such a broad spectral range. Therefore the experiment has to be performed with a phase retarder having phase shift varying in a range $0 < \delta < \frac{\pi}{2}$. Then the spectrum of Kerr ellipticity is calculated from (3.13) - (3.16) using already measured spectrum of Kerr rotation.

At the end of this chapter let us only briefly add a few words about MO spectroscopy of the Faraday effect which is also partially employed in this work.

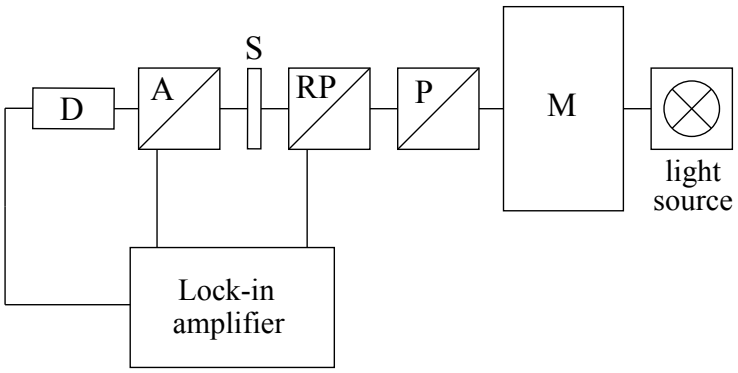

Figure 3.4: Basic diagram of spectrometer for Faraday rotation measurements; A - analyser, D - detector, M - monochromator, P - polariser, RP - rotating polariser, S - sample.

A simplified diagram of the used Faraday spectrometer is shown in Fig. 3.4. Basic principle of this spectrometer is very similar to the Kerr spectrometer introduced above. The main difference lies in the way of modulation. In the previous case the Faraday modulation cell is used, while here a rotating polariser or a rotating phase retarder takes place. The method uses analogical compensation principle with the feedback loop. The detected signal, which is processed in the lock-in amplifier controls the orientation of the analyzer and therefore it compensates the MO effect of the investigated sample.

As a light source, a combination of Xe and halogen lamp is used allowing measurements from near ultraviolet to near infrared spectral region. For detection we employ photomultiplier, silicon photodiode and cooled PbS detector covering a spectral range from approximately 0.5 eV to 5.0 eV. Faraday rotation measurement is performed using set-up with a rotating polariser depicted in Fig. 3.4. Spectra of MCD are obtained with an additional phase retarder and rotating phase retarder instead of the rotating polariser. Both configurations allow us to perform high precision measurements and are able to detect MO effects in order of thousandths of degrees.

4. Investigated samples

4.1 $La_{2/3}Sr_{1/3}MnO_3$

The recently extensively developing field of spintronics requires materials with specific properties allowing the control of their spin behaviour. Among such materials hole doped manganites $La_{1-x}M_xMnO_3$ (M=Ca, Sr, Ba) with perovskite-type structure are promising candidates, even though the first studies of their exceptional properties had already been done several decades before the spintronics field emerged in the 1980s.

The first experimental observation of CMR phenomenon in manganese oxides had already been performed at the beginning of the 1950s by Jonker and van Santen [36, 74], followed by its theoretical explanation via DE interaction by C. Zener [86]. Furthermore, next experimental [34, 82, 35] and theoretical [20, 1, 19] studies of their basic physical properties shown that varying of x could lead to both ferromagnetic and antiferromagnetic behaviour. This was also theoretically explained by DE interaction.

A renewed interest in these materials came in the 1990s after the observations of CMR in La-Ba-Mn-O [24] and La-Ca-Mn-O [33], because the CMR and extremely high degree of spin polarization make manganese oxides very promising from the application point of view. Therefore numerous studies about their properties have followed in the last two decades. Among them considerations about the influence of lattice effects and non-stoichiometry on the DE interaction and overall properties [26, 72, 60, 58, 59, 23]. Approaches different from conventional substitution of La [46]. Studies of electronic structure and related phenomena [12, 56, 61, 15]. Insufficiency of the DE interaction to completely describe the observed characteristics [44]. Comparison to other CMR materials [55] and also investigations of the optical properties [37, 49, 67, 71, 41]. Also several MO studies of LSMO were performed using MO Kerr spectroscopy at both room [18, 83, 48, 40, 45, 76] and low temperatures [57].

All this extensive research has provided better insight into the origin and character of the physical properties and it has contributed to a proposal of the electronic structure lying behind it. However, many effects arising in thin films of these materials still remain unclear. One of them is reported [66, 81] change in physical properties of ultrathin films (thickness ≤ 10 nm) in comparison to bulk materials. Since manifesting itself in ultrathin layers, it is considered to originate at the LSMO/STO interface. However details of this effect have not been clarified yet. In order to understand the possible mechanisms let us say a few words about the crystallographic and electronic structure.

An ideal crystallographic structure of manganese oxide is cubic perovskite. Nevertheless, in reality the samples do not undergo an ideal growth process and distorted rhombohedral or orthorhombic structure occurs. Films investigated in this work feature the case of orthorhombic structure (see Fig. 4.1).

Taking look at the energy levels of an isolated $3d$ ion we have five degenerated orbital states, however in a crystal field these are all split into three t_{2g} and two e_g orbitals as shown in Fig. 4.2. The distinct characters of individual orbitals are shown as well. Usually the two types of e_g orbitals, $(3z^2 - r^2)$ and $(x^2 - y^2)$, are

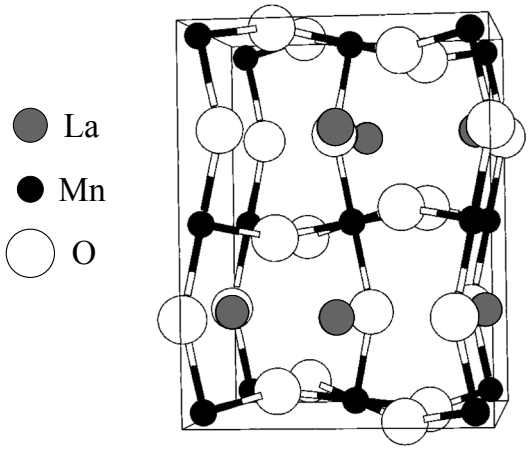

Figure 4.1: Distorted orthorhombic structure of the LSMO parent compound $LaMnO_3$ [52].

not occupied by the Mn^{3+} electrons randomly and an orbital ordering is achieved.

The magnetic properties of manganese oxides are driven by the manganese ion spins and their mutual exchange interactions, which are given by the overlap of the manganese d-orbitals and the oxygen p-orbitals. In case of Mn^{4+}-O-Mn^{4+} molecules superexchange interaction takes place giving rise to antiferromagnetic behaviour, for Mn^{3+}-O-Mn^{3+} the superexchange can be both ferromagnetic or antiferromagnetic.

In case of mixed valence Mn^{3+}-O-Mn^{4+} (which is our case) a different situation occurs. A mechanism introduced by C. Zener [86] and called double exchange interaction probably got its name because of the two simultaneous electron jumps involved it this process. As shown in Fig. 4.3 an electron transition from $2p$ orbital of the anion O^{2-} is accompanied by a jump of the e_g electron of the Mn^{3+} on the just emptied place. The probability of DE transitions strongly depends on the geometry of the Mn^{3+}-O-Mn^{4+} bonding, i.e. the length of Mn-O bond and the Mn^{3+}-O-Mn^{4+} bond angle. Therefore one of the main factors responsible for changes in the magnetic ordering is strain arising in the layer due to lattice mismatched substrate used for the deposition [21].

Even though LSMO/STO interface effects have been recently extensively investigated, the influence of the strain on the resulting properties has not been

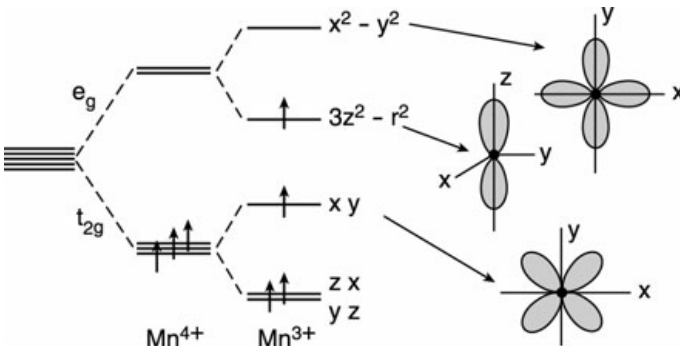

Figure 4.2: Diagram of energy level splitting in a crystal field for Mn^{3+} and Mn^{4+} ions with corresponding orbitals [21].

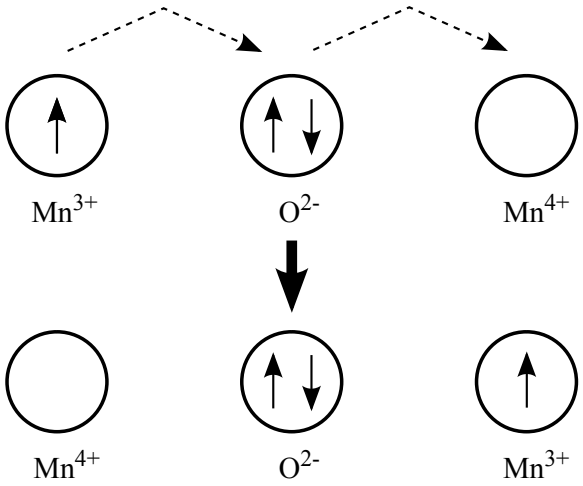

Figure 4.3: Diagram of DE interaction.

satisfactorily explained yet. Also because there have appeared even studies with results in clear contradiction. The research group of Tebano et al. has recently reported that broken symmetry at the interfaces leads in a stabilization of the out-of-plane manganese e_g $(3z^2 - r^2)$ orbitals against the in-plane e_g $(x^2 - y^2)$ orbitals, which results in a suppression of the DE interaction [68, 69]. Whereas the group of Huijben et al. in contrary refers to an observation of preferred orbital ordering of the e_g $(x^2 - y^2)$ orbitals [25]. Since all these studies were performed on sets of samples with various thicknesses and with no depth sensitivity, there is still missing a clear experimental evidence in the ferromagnetic behaviour of the ultrathin layers. A recent theoretical study [42] proposed a model of gradual restoration of DE interaction in the first few monolayers (ML) of ultrathin films (thickness < 10 ML). In this work we try to provide an experimental verification of the proposed mechanism.

The investigated samples of LSMO were prepared by a research group of Ph. Lecoeur[1] on STO substrate with (100) crystallographic orientation employing PLD. An ultraviolet ($\lambda = 248$ nm) KrF laser was used with the pulse repetition rate of 1 Hz and maximum energy fluence 3 J/m^2. The substrate was maintained at 620 °C and the oxygen pressure reached 120 mTorr. Such parameters led to optimal single-crystalline layer growth. The lattice parameters are $a_{LSMO} = 3.889$ Å and $a_{STO} = 3.905$ Å, giving lattice mismatch circa 0.41 %. The thickness range of prepared films is from 103.9 down to 5.0 nm (measured by X-ray diffraction). Improvement of the interface quality and surface smoothness was achieved by a beam homogenizer - a spatial filter for the laser beam. Surface roughness bellow 0.2 nm (measured by atomic force microscopy) was reached this way.

4.2 $\mathbf{Ce_{1-x}Co_xO_{2-\delta}}$

Another group of magnetic oxides has attracted attention thanks to recently appeared new device concepts in the field of photonic technologies, which are employing MO effects. These have been for example MO isolators [62, 7, 65],

[1]Institut d'Electronique Fondamentale, Université Paris-Sud XI, 91405 Orsay Cedex, France

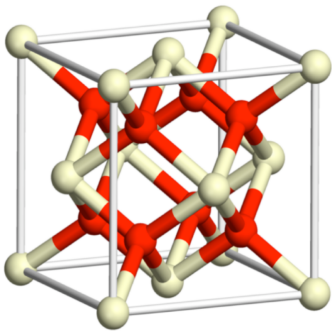

Figure 4.4: Schematic crystallographic structure of CeO_2 [63]. White spheres represent cerium and red spheres oxygen.

magneto-photonic crystals [28, 50, 39, 30, 29], MO spatial light modulators [31, 32] or magneto-plasmonic crystals [6, 5, 4, 53]. Such devices are in demand for many commercial applications, however there are several technological difficulties preventing their widespread use. The most problematic issues limiting large-scale expansion are both material integration and design of the devices. Therefore there has been a seek for new materials with suitable physical properties and simultaneously with a good silicon compatibility necessary for proper integration.

One of such materials has appeared to be magnetically doped CeO_2. It shows high Curie temperature [80, 16], possibility of tuning its properties by Co doping [70] and also very good compatibility with silicon technology [8]. A crystallographic structure of pure CeO_2 is fluorite with lattice constant of 5.411 Å. In Fig. 4.4 is shown its unit cell with four cerium and eight oxygen atoms. A schematic band diagram of pure CeO_2 is depicted in Fig. 4.5. It displays the prominent oxygen and cerium states together with approximate energies of the electron transitions. Their contributions to optical and MO spectra will be further discussed in the chapter dedicated to experimental results.

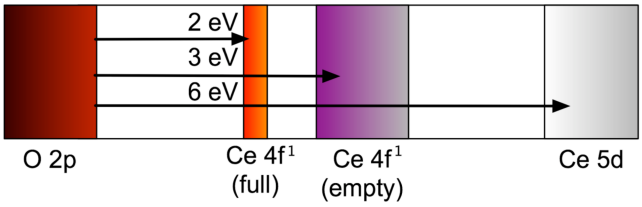

Figure 4.5: Schematic band diagram of CeO_2 containing defects. Ce $4f^1$ (full) is missing without defect states [9].

Although several experimental investigations of Co doped CeO_2 have been done as well as a few theoretical studies a more complex understanding of the origin and mechanism of the observed ferromagnetic properties still remain unexplained. The knowledge of optical and MO properties is missing as well. Therefore more detailed studies providing deeper understanding and characterization should be done in order to successfully employ this promising material in a large-scale use. In this work we try to perform a systematic and thorough investigation of optical and MO properties of Co doped CeO_2 thin films in order to provide the necessary missing information.

Research group of C. A. Ross[2] prepared the samples of magnetically doped $Ce_{1-x}Co_xO_{2-\delta}$ films (x = 0.05, 0.10 and 0.20) investigated in this work. They were grown by PLD on MgO substrate with (100) crystallographic orientation except of the sample of x = 0.20 which was grown on oxidized Si (100). The deposition vacuum reached 10^{-6} Torr, substrate was heated at 700 °C. Such conditions led to textured polycrystalline films with out-of-plane easy axis and grain size from 40 to 100 nm. Thicknesses of the samples are 753, 262 and 391 nm for the samples of x = 0.05, 0.10 and 0.20 respectively (measured by profilometer).

[2]Department of Materials Science and Engineering, Massachusetts Institute of Technology, MA 02139 Cambridge, USA

5. Experimental results

5.1 Magneto-optical Kerr spectroscopy of $La_{2/3}Sr_{1/3}MnO_3$

All the experimental data presented in this section were obtained using MO spectrometer based on azimuth modulation technique which was introduced in the third chapter. The main components of the spectrometer were 450W Xe arc lamp, quartz prism monochromator, calcite prism polariser and analyser and quartz glass dc compensating and ac modulating cell. Measured signal was detected by photomultiplier.

5.1.1 Polar configuration

The spectra measured in polar geometry (see Fig. 2.1) were obtained at nearly normal light incidence. The samples were placed in a magnetic field of 1.2 T sufficient for their magnetic saturation as was verified by hysteresis loops measurements. Measured spectral range was from 1.2 eV to 4.8 eV. The experiments were performed at room temperature.

We begin the presentation of results with brief overview of the whole series of investigated samples and introduction of their characteristic features before focusing on the interface phenomena. Fig. 5.1 shows the polar Kerr rotation spectra of four samples with largest thicknesses. We can see two prominent spectral features - the maximum at energy approximately 2.7 eV and the minimum at around 3.6 eV. It was shown [83] that the former spectral peak is probably related to a dipole-forbidden spin-allowed intra-3d-Mn crystal field electron transition and the later to a charge-transfer transition from O^{2-} $2p$ to Mn^{3+} $3d$ e_g orbital. These assumptions have been recently verified by several theoretical calculations [43, 73]. Besides these two prominent features spectra of the two

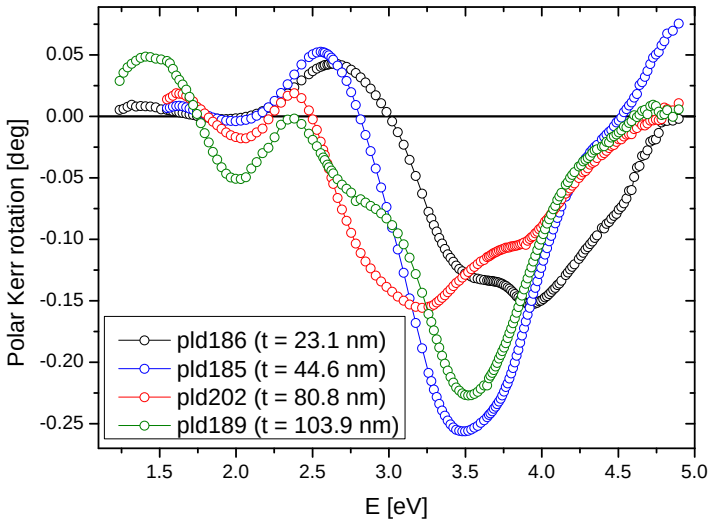

Figure 5.1: Polar Kerr rotation spectra of four samples with the largest thicknesses.

thickest samples (t = 80.8 and 103.9 nm) display certain irregularities. Their origin has not been fully clarified, however it is expected [85] that the growth is not optimal over circa 40 nm and therefore it can lead to a structure distortion in an unknown way. Because of these irregularities we do not consider the two thickest samples as typical examples of LSMO layers and we will not involve them in further discussion.

We can also notice that the spectrum of 23.1 nm thick layer shows splitting of the spectral minimum at around 3.8 eV, which is even more visible in Fig. 5.2, which displays the polar Kerr rotation spectra of the thinnest samples. It was shown [85, 77] that this effect observed only in ultrathin layers (t $\leq$ 20 nm) originates from a backside reflection on the STO substrate in combination with a small ($\sim$ 30 nm) penetration depth at the given energy. Nevertheless, we see that all three samples, including the thinnest one, display spectral behaviour typical for LSMO films, which is a clear evidence of magnetic ordering down to five nanometers of layer thickness.

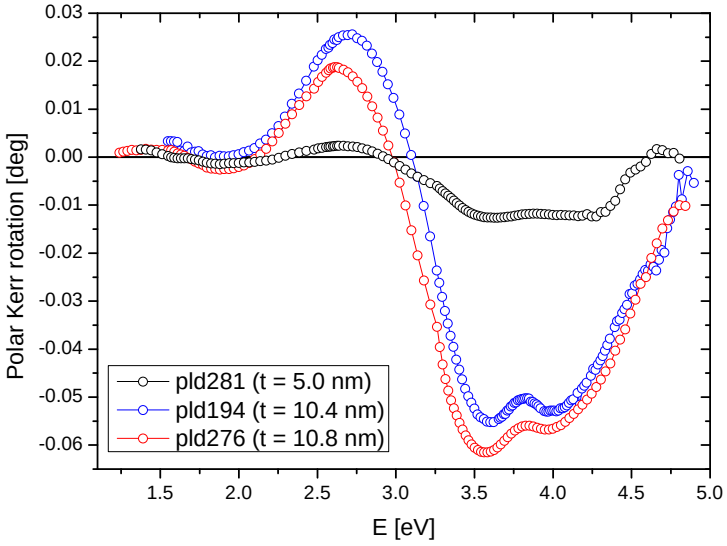

Figure 5.2: Polar Kerr rotation spectra of the three thinnest samples.

Fig. 5.3 shows five spectra of polar Kerr ellipticity representing all the samples we consider to be typical for LSMO. The two spectral peaks, described in the Kerr rotation spectra, are now visible as well. They display an energy shift so that the rotation and ellipticity are in a consistency with Kramers-Kronig relations. Besides the thickness dependence of the MO effect amplitude we can observe also thickness dependent energy shifting of the main peak ($\sim$ 3.4 eV).

The theoretical calculations in this section are based on transfer matrix formalism introduced in the second chapter. A model assuming a single layer on semi-infinite substrate was considered, since it has proved itself [85, 77] to be reasonable approximation in this case. Bulk-like material parameters used for the calculations (diagonal and off-diagonal components of the permittivity tensor) were obtained [75] on a 35 nm thick LSMO layer on STO (100) substrate. The substrate optical parameters (diagonal components of the permittivity tensor) were adopted from spectroscopic ellipsometry (SE) performed on bare STO [45].

As a brief introduction into the theoretical models let us present a comparison between experimental and calculated data for the samples pld186 (t = 23.1 nm)

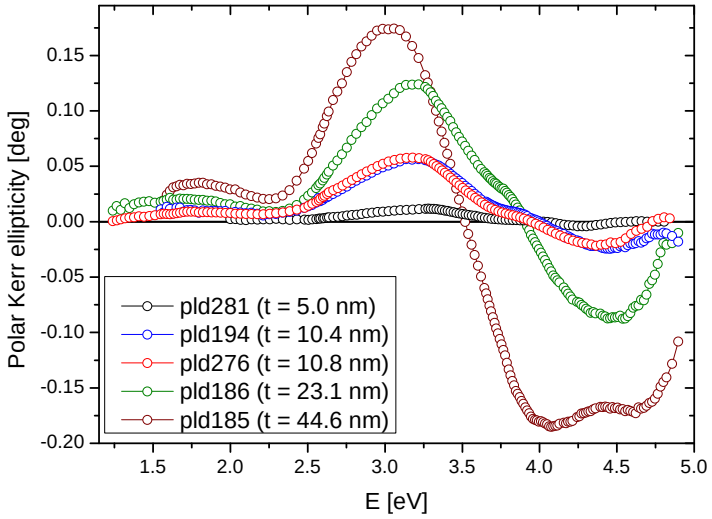

Figure 5.3: Polar Kerr ellipticity spectra of all characteristic LSMO layers in the investigated series of samples.

and pld185 (t = 44.6 nm), which is displayed in Fig. 5.4. We can see an excellent agreement between theory and experiment in the whole spectral range. This tells us that both samples manifest characteristic LSMO behaviour, overall high quality and bulk-like magnetic properties. For the calculations were even used higher expected thicknesses since the original ones were not sufficient for such precise description, which is evident in Fig. 5.4. This can be considered as a clear evidence of achieved improvement in the deposition process.

Another theoretical calculation is shown in Fig. 5.5. It displays MO properties of 10.8 nm thick sample compared with the model spectrum calculated from bulk-like parameters. Once again there is an evident agreement between experimental and calculated data. A small deviation in the UV region, which is

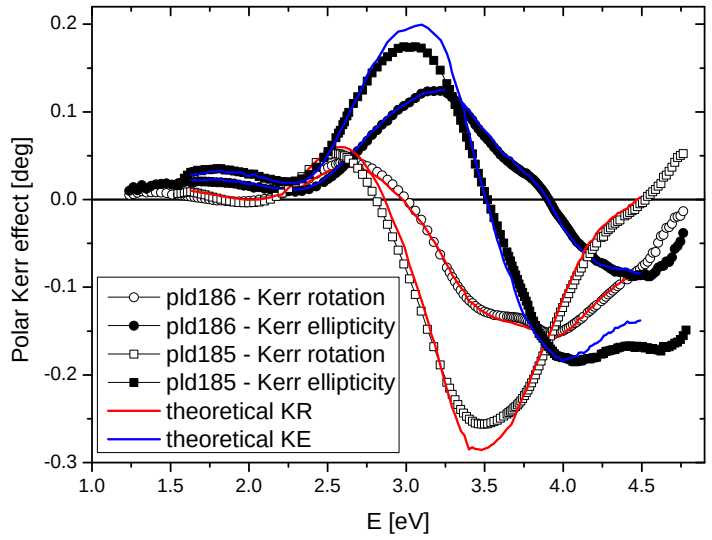

Figure 5.4: Experimental and theoretical spectra of polar Kerr effect of two samples pld186 (t = 23.1 nm) and pld185 (t = 44.6 nm). Calculations were performed using bulk-like material parameters and thicknesses of 28.0 and 55.0 nm.

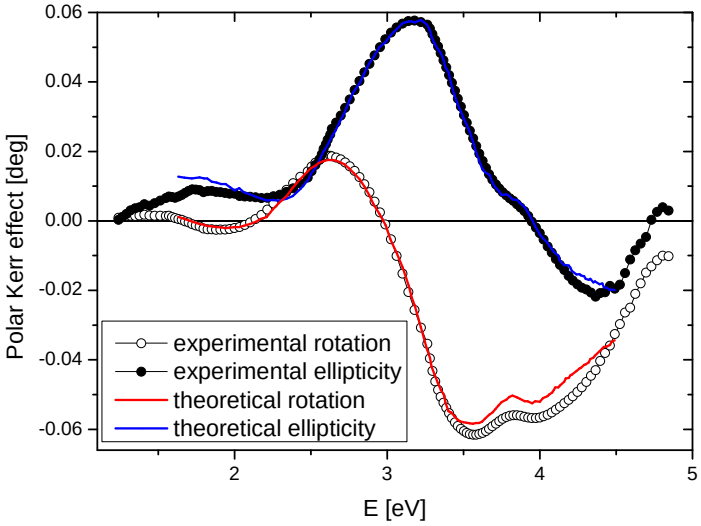

Figure 5.5: Comparison of experimental polar Kerr effect of 10.8 nm thick film (pld276) with theoretical calculations employing bulk-like permittivity tensor elements of 35.2 nm thick LSMO layer.

visible mainly in the Kerr rotation spectrum can be ascribed to more sensitive photomultiplier used in the experiment. In comparison to the previous measurements a photomultiplier with enhanced UV sensitivity was used. Insensitivity of the older detector in UV region resulted in lower amplitude of MO parameters, which were used in the theoretical calculations. Because of such good agreement between theory and experiment we can conclude that layer/substrate interface phenomena are not yet important at this thickness and that the MO properties are very close to bulk ones.

Fig. 5.6 displays polar Kerr effect measurements together with two types

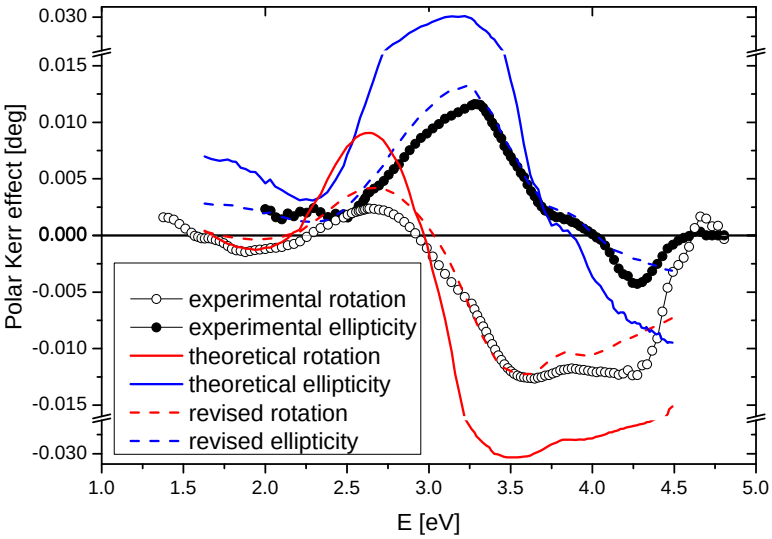

Figure 5.6: Experimental and theoretical data of polar Kerr effect of the 5.0 nm thick LSMO film. Solid curves display model structure of single layer on a semi-infinite substrate with bulk-like LSMO material parameters. Dashed curves represent more realistic model shown in Fig. 5.7.

of theoretical calculations for the thinnest sample of 5.0 nm. The experimental data manifest features characteristic for LSMO layers and therefore reveal ferromagnetic ordering down to 5.0 nm. The first theoretical model was calculated using the same material parameters and structure of one layer on semi-infinite substrate as for the thicker samples (in Fig. 5.6 depicted as solid curves). We can see similar spectral dependences compared to the experimental data but also obvious difference in the MO effect amplitudes. That is the case where the interface effects need to be considered and more realistic structure to be employed.

In our next calculations we tried to follow recently suggested mechanism of suppressed DE interaction at the LSMO/STO interface [68, 69]. This mechanism originates in broken symmetry at the interface, which is accompanied by stabilization of the out-of-plane e_g $(3z^2 - r^2)$ orbitals and results in the suppression of the DE interaction. Recently, there has been proposed more detailed theoretical model [42] assuming this preferred orbital ordering in close vicinity of the interface in the first three MLs of the film. In the next ML the preferred $(3z^2 - r^2)$ ordering starts to relax towards more balanced $(x^2 - y^2)$, which is followed by an increase of T_C and gradual evolution of DE interaction. This is supposed to continue until the eighth ML where T_C becomes saturated and DE fully restored.

Adopting this model we tried to create a more realistic model structure of the LSMO layer, which would better describe the experimental data. Fig. 5.7 shows such model structure, which consists of 6 monolayers thick LSMO layer with no DE and therefore no magnetic ordering followed by region of increasing DE until the ninth ML. The last 4 MLs contain fully restored DE and therefore bulk-like ferromagnetic ordering. Whole structure is placed on semi-infinite STO substrate. A corresponding DE intensity was achieved by modification of the off-diagonal permittivity tensor components of LSMO.

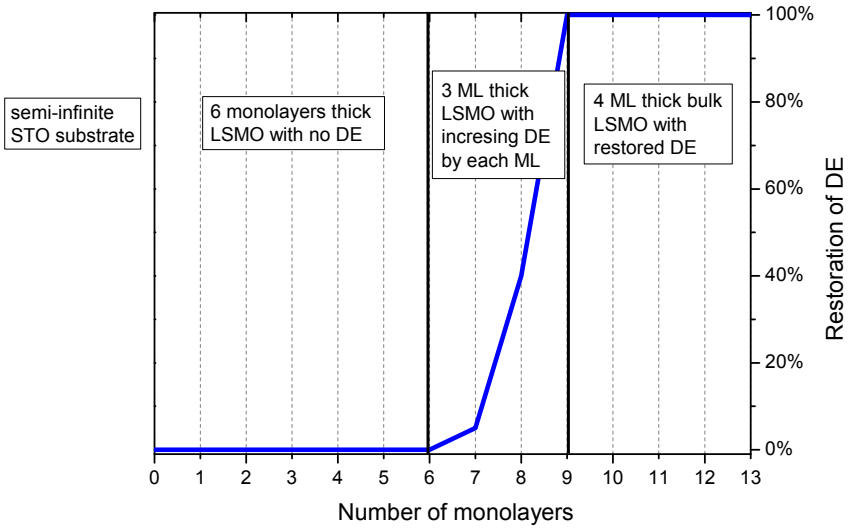

Figure 5.7: A realistic model of evolution of DE interaction in 5.0 nm thick LSMO film deposited on STO substrate.

Calculations based on this model are displayed in Fig. 5.6 as dashed curves. We can see an evident agreement between the experimental data and revised theoretical calculations which is a clear evidence of the DE evolution process inside the ultrathin LSMO films. Consistently with the recently proposed model

[42] we assume that the $(3z^2 - r^2)$ orbital ordering suppressing DE interaction starts to relax after first 3 ML of the sample, however at room temperature we observe no ferromagnetic ordering until the sixth ML because the intensity of DE is too small. Low temperature measurements could possibly provide better insight into this complex and problematic issue.

5.1.2 Longitudinal configuration

Experimental spectra measured in longitudinal geometry (see Fig. 2.1) were obtained at the angle of light incidence of 56 degrees for p-polarized incident wave. Investigated spectral range was from 1.2 eV to 4.8 eV. External magnetic field of 0.25 T was sufficient for magnetic saturation of the samples. The experimental data were taken at room temperature.

As an introduction to the longitudinal geometry let us present spectra of Kerr rotation (see Fig. 5.8) showing again behaviour typical for LSMO layers with two characteristic features at energies 2.7 and 3.6 eV. Amplitudes of the MO effect are naturally lower than in the polar geometry. Nevertheless we can still clearly see the thinnest sample displaying MO effect as a confirmation of its ferromagnetic properties. In the spectra we can also notice that the splitting of the minimum for the thinnest samples around 3.8 eV is not as clear as in the polar configuration. This is natural to expect since the broadening is caused by the reflection on STO substrate and in longitudinal configuration the path of light through the layer is increased due to the non-zero angle of incidence.

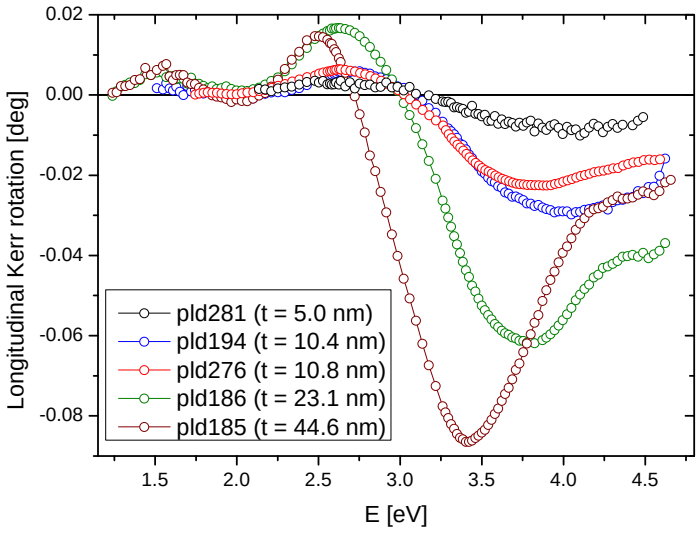

Figure 5.8: Longitudinal Kerr rotation spectra in case of p-polarized incident wave and angle of incidence 56°.

Fully developed LSMO features are visible also in the Kerr ellipticity spectra, which are shown in Fig. 5.9. We can notice higher level of noise in the spectra taken on the two thinnest samples (t = 10.4 and 10.8 nm). The Kerr ellipticity spectrum of the thinnest sample is missing, because it is already beyond the spectrometer sensitivity.

Theoretical models were calculated analogically to the polar case using the same material parameters and model structures. Fig. 5.10 shows comparison

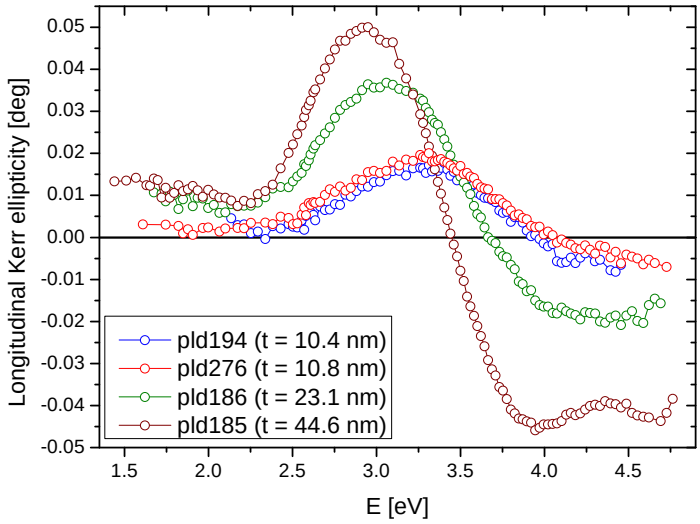

Figure 5.9: Longitudinal Kerr ellipticity spectra in case of p-polarized incident wave and angle of incidence 56°. Spectrum of the thinnest sample (t = 5.0 nm) is missing because it is already beyond the edge of the used experimental set-up.

of the experimental data with theoretical calculations for 10.8 nm thick LSMO film. An agreement in spectral behaviour is well visible although there is a small difference in the effect amplitudes. This can be probably ascribed to slightly higher measurement temperature (circa 10 K difference) caused by different electromagnet cooling in the polar and longitudinal configuration. Even such a small variation can lead to observable changes since the ferromagnetic properties of LSMO layers strongly depend on temperature near T_C.

Fig. 5.11 shows experimental longitudinal Kerr rotation spectrum of the thinnest sample of 5.0 nm thickness together with a theoretical calculation based on a model structure introduced in Fig. 5.7 considering the gradual evolution of DE

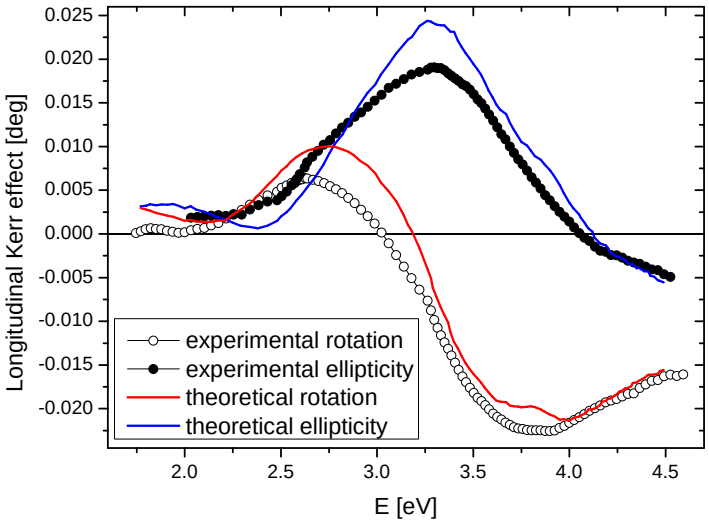

Figure 5.10: Experimental and theoretical spectra of longitudinal Kerr effect of 10.8 nm thick LSMO layer in case of p-polarized incident wave and angle of incidence 56°. The theoretical calculation were performed using bulk-like material parameters of 35.2 nm thick LSMO layer.

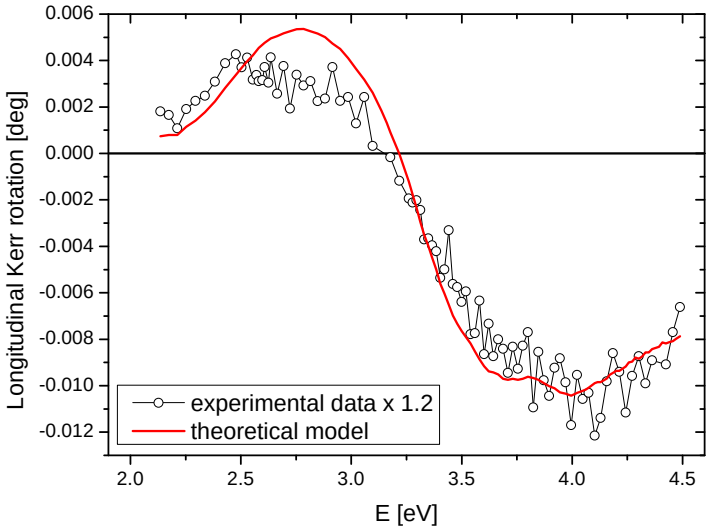

Figure 5.11: Comparison of experimental longitudinal Kerr rotation spectrum of the thinnest sample (t = 5.0 nm) with a theoretical calculation performed using bulk-like LSMO material parameters and model structure shown in Fig. 5.7. The spectra are for p-polarized incident wave and angle of incidence 56°.

interaction. A reasonable agreement between theory and experiment proved the proper usage of our model structure. The difference in the effect amplitudes can be again attributed to the higher measurement temperature as well as to the experimental error of such small effect. Because of the high level of noise we can see that values in order of millidegrees are at the edge of the set-up sensitivity. Nevertheless, Fig. 5.11 provides once more a clear evidence of ferromagnetic ordering down to 5.0 nm of film thickness as well as the confirmation of the proposed LSMO/STO interface mechanism with gradual restoration of the DE interaction.

5.2 $Ce_{1-x}Co_xO_{2-\delta}$

5.2.1 Spectroscopic ellipsometry

Measurements of ellipsometry data together with their numerical analyzes were made with a great help of J. Mistrík[1]. The experiment was performed using a high precision Woollam VASE ellipsometer in the spectral range from 1 to 5 eV. Three angles of incidence were chosen - 65°, 70° and 75°. Optical reflectivity and transmission spectra were measured using the same ellipsometer and analyzed together with the ellipsometry data assuming a model structure consisting of a $Ce_{1-x}Co_xO_{2-\delta}$ homogeneous layer covered with a rough surface layer and placed on an MgO substrate. The spectral shape of the diagonal component of the permittivity tensor was parametrized by the sum of damped Lorentz and Tauc-Lorentz oscillators. The least square method was used to adjust the parameters of the oscillators as well as the film thicknesses and surface roughness.

The spectra of the real part of the diagonal permittivity tensor element are

[1]Faculty of Chemical Technology, University of Pardubice, 53210 Pardubice, Czech Republic

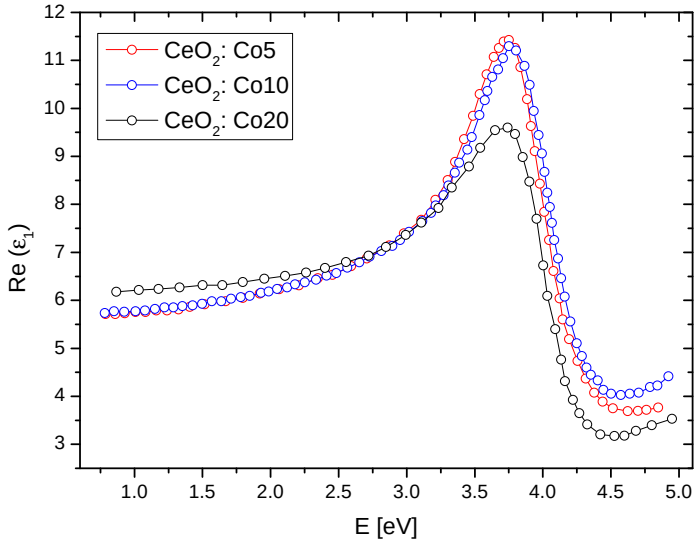

Figure 5.12: Spectra of the real part of the diagonal component of the permittivity tensor of $Ce_{1-x}Co_xO_{2-\delta}$ films for x = 0.05, 0.10 and 0.20, which were derived from ellipsometry data.

shown in Fig. 5.12. The spectral behaviour is similar to results obtained on pure CeO_2 films [3] and the fit revealed two optical transitions at around 3.9 and 8.1 eV. These are related to charge transfer from O $2p$ states to Ce $4f$ and Ce $5d$ states [3]. The bandgap energies were estimated to be approximately $E_g \sim 3.25$ eV for $Ce_{0.95}Co_{0.05}O_{2-\delta}$ (Co5) and $E_g \sim 3.21$ eV for $Ce_{0.90}Co_{0.10}O_{2-\delta}$ (Co10). These values are in a good agreement with bandgap energies $E_g \sim (3.23 \pm 0.05)$ eV of pure CeO_2 films fabricated by radio frequency sputtering [11].

On the other hand results of the imaginary part of the diagonal component of the permittivity tensor (see Fig. 5.13) show noticeably larger amplitudes compared to the pure CeO_2 films. Such results therefore indicate stronger absorption

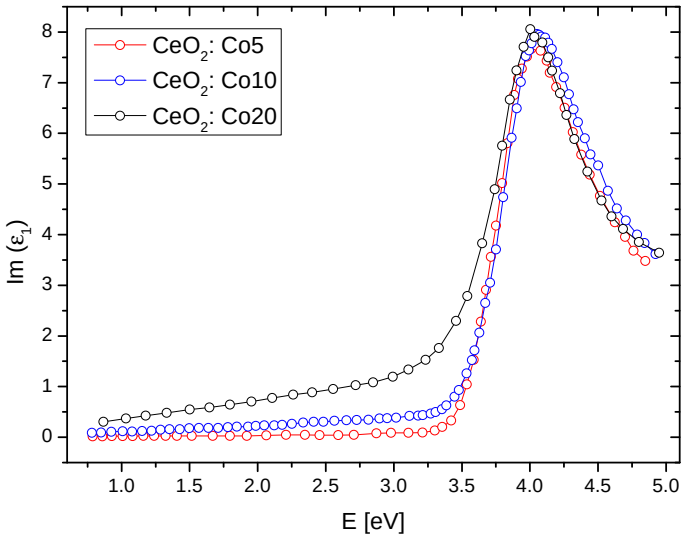

Figure 5.13: Spectra of the imaginary part of the diagonal component of the permittivity tensor of $Ce_{1-x}Co_xO_{2-\delta}$ films for x = 0.05, 0.10 and 0.20, which were derived from ellipsometry data.

in cobalt doped samples. In Fig. 5.13 we can also see that the amplitude increases in the whole spectral range with increasing cobalt doping, which indicates a dependence of optical properties of CeO_2 films on cobalt content.

5.2.2 Magneto-optical spectroscopy

Experimental data from both Faraday and Kerr magneto-optical spectroscopies are presented in this section. Spectrometers used for the measurements are described more in detail in the third chapter. The Faraday rotation (FR) and magnetic circular dichroism (MCD) spectra were measured in a spectral range from 0.5 eV to 3.8 eV. The MO Kerr effect measurements were performed at room temperature in polar configuration at nearly normal light incidence in a spectral range from 1.2 eV to 4.8 eV. The external magnetic field of 0.6 and 1 T in the Faraday and the Kerr configuration, respectively, were sufficient for saturation of the samples. The obtained FR spectra were corrected for the MgO substrate contribution.

In Fig. 5.14 we can see MCD hysteresis loops measured at room temperature (RT) and photon energy of 3.3 eV. A RT ferromagnetic behaviour is clearly visible as well as a dependence of resulting MO properties on the cobalt content. Saturation magnetization, coercivity and saturation remanence increase with increasing cobalt doping. The Co5 sample hysteresis loop shows almost zero coercivity whereas the Co10 hysteresis loop exhibits typical magnetic anisotropy with out-of-plane easy axis. In-plane magnetization is impossible to saturate even at 1 T.

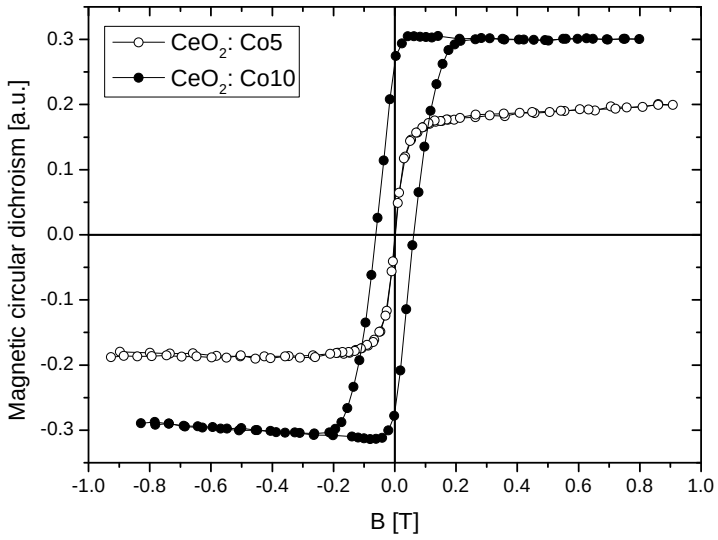

Figure 5.14: Hysteresis loops of magnetic circular dichroism of $Ce_{1-x}Co_xO_{2-\delta}$ films for x = 0.05 and 0.10. Measured at room temperature and photon energy of 3.3 eV.

Room temperature FR spectra are displayed in Fig. 5.15. The spectral behaviour shows interference indicating multiple reflections inside the samples. There are two characteristic features. A spectral minimum at energy circa 1.1 eV and a spectral maximum at around 3.5 eV. The dependence of MO properties on the cobalt content is clearly visible. The FR amplitude of the sample Co10 is remark-

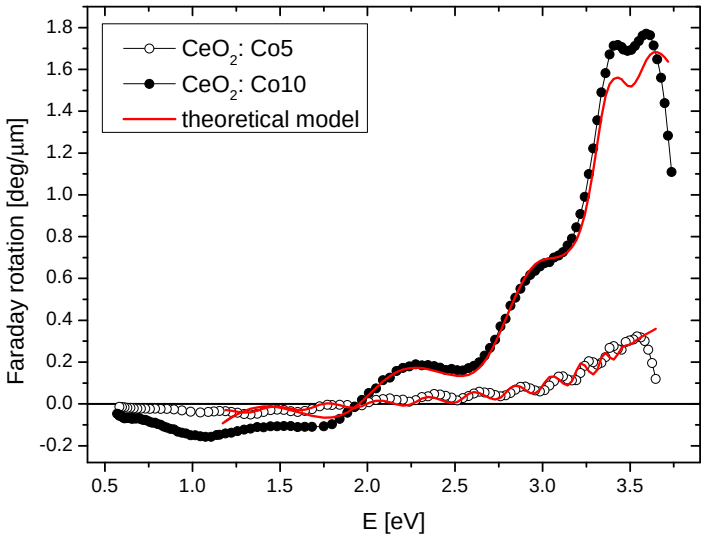

Figure 5.15: Experimental and theoretical spectra of Faraday rotation of $Ce_{1-x}Co_xO_{2-\delta}$ films for x = 0.05 and 0.10. The measured data are corrected for MgO substrate contribution. Theoretical spectra are fitted using two paramagnetic transitions.

ably higher in the whole spectral range and near the optical band edge is even approximately five times larger than the amplitude of Co5. A higher amplitude of MO effect is clearly visible in the whole investigated spectral range also in the MCD spectra shown in Fig. 5.16.

The experimental data in Fig. 5.15 and 5.16 together with already calculated diagonal permittivity tensor components (see Fig. 5.12 and 5.13) served for numerical calculations to derive the off-diagonal permittivity tensor element of the investigated samples. The spectra were parametrized by a sum of two paramagnetic transitions (2.13) with opposite signs. The transition energies were

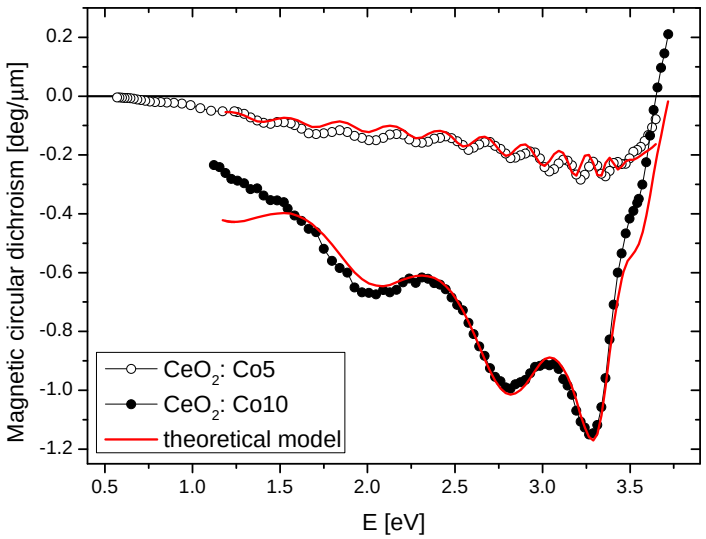

Figure 5.16: Experimental and theoretical MCD spectra of $Ce_{1-x}Co_xO_{2-\delta}$ films for x = 0.05 and 0.10. Theoretical spectra are fitted using two paramagnetic transitions.

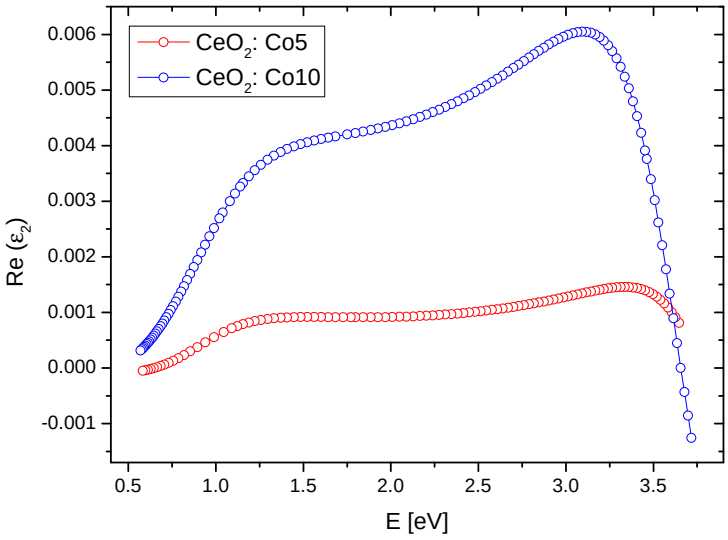

Figure 5.17: Spectra of the real part of the off-diagonal component of the permittivity tensor of $Ce_{1-x}Co_xO_{2-\delta}$ films for x = 0.05 and 0.10. Fitted from the Faraday effect spectra.

estimated at approximately 0.90 and 3.77 eV for the Co5 sample and 0.87 and 3.63 eV for the Co10 sample. Based on studies of cobalt ferrites, the former one was reported [17] to be a crystal field (CF) transition of Co^{2+} between $^4A_2$ and $^4T_1$ states. The later one was observed [3] at similar energies in pure CeO_2 and identified as a charge transfer (CT) from O $2p$ states, in our case to Co $3d$ states. The oscillator amplitudes $(\varepsilon_2'')_{max}$ were computed to -0.0009 and 0.0026 for Co5 sample and -0.0036 and 0.0109 for the Co10 sample. The amplitudes of the CF transition are significantly lower compared to these of the CT transition, as can be expected, since the transition is parity forbidden. However, a tensile strain in the layer results in a broken symmetry and the transition can be observed.

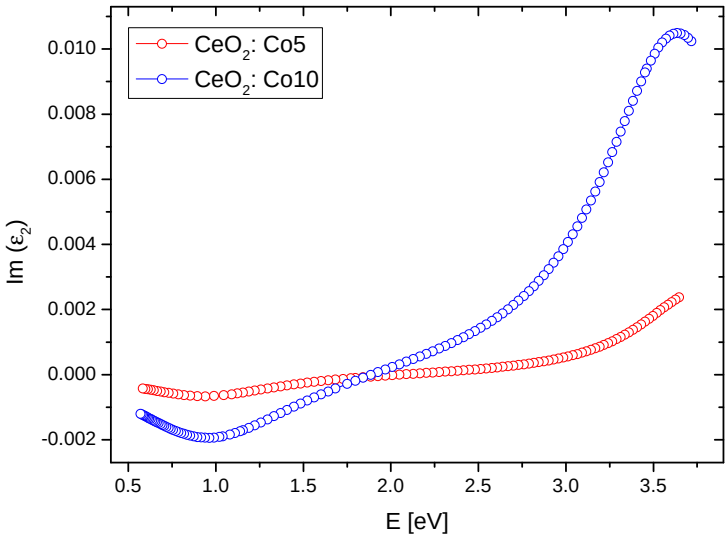

Figure 5.18: Spectra of the imaginary part of the diagonal component of the permittivity tensor of $Ce_{1-x}Co_xO_{2-\delta}$ films for x = 0.05 and 0.10. Fitted from the Faraday effect spectra.

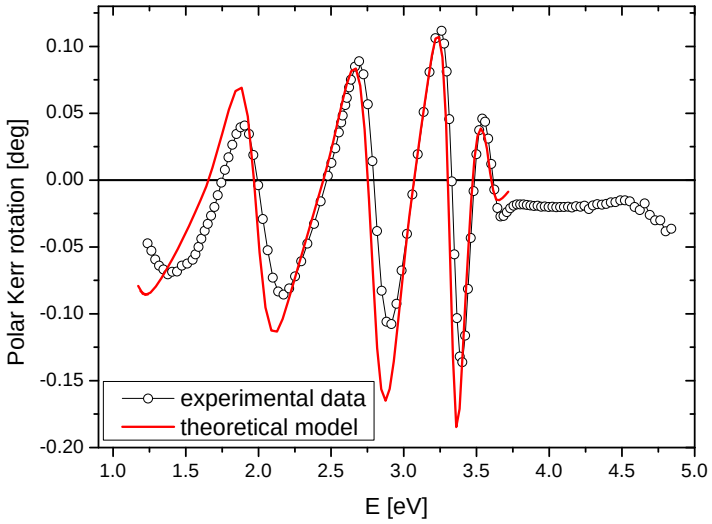

Figure 5.19: Comparison of experimental polar Kerr rotation of the $Ce_{0.90}Co_{0.10}O_{2-\delta}$ sample with a theoretical model. The spectrum was obtained at nearly normal light incidence and room temperature. The theoretical data were calculated using material parameters computed from ellipsometry and Faraday effect measurements.

Although the oscillator strength still remains very small in comparison to the CT transition. The corresponding spectral behaviour of the real and imaginary part of the off-diagonal permittivity tensor element is shown in Fig. 5.17 and 5.18.

The fitted model spectra of Faraday effect are shown together with experimental data in Fig. 5.15 and 5.16. A very good agreement between the theory and experiment confirms a proper calculation of the permittivity tensor elements.

The validity of calculated material parameters was further examined by MO

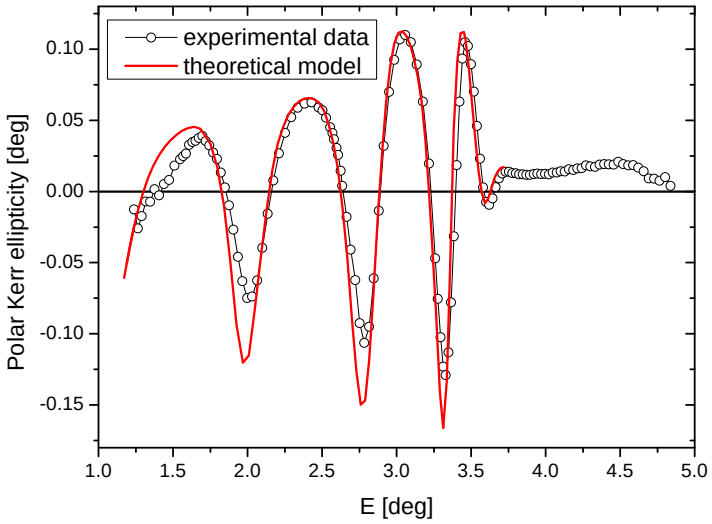

Figure 5.20: Comparison of experimental polar Kerr ellipticity of the $Ce_{0.90}Co_{0.10}O_{2-\delta}$ sample with a theoretical model. The spectrum was obtained at nearly normal light incidence and room temperature. The theoretical data were calculated using material parameters computed from ellipsometry and Faraday effect measurements.

Kerr spectroscopy. Experimental spectra of Kerr rotation and Kerr ellipticity of the Co10 sample are shown in Fig. 5.19 and 5.20 together with theoretical calculations, which used obtained material parameters. A very good agreement between theoretical and experimental data is clearly visible confirming the proper spectral dependence of derived elements of the permittivity tensor.

The last step performed to verify the validity of the obtained material parameters was investigation of a possible temperature dependence of the observed effects. Since we have determined the two transitions responsible for MO behaviour as paramagnetic transitions, we should observe no temperature dependence of the MO effects. Therefore we performed low temperature measurements of Faraday effect of the Co10 sample. The experiment was carried out using cryostat cooled by liquid nitrogen, thus the temperature of the sample was maintained at approximately 80 K. The spectra of both low and room temperature measurements are shown in Fig. 5.21. In the whole investigated energy range we can see an agreement in the spectral behaviour as well as in the amplitudes of the Faraday rotation and MCD giving a clear evidence of no temperature dependence of the investigated phenomena. This can be considered as another verification of our theoretical model.

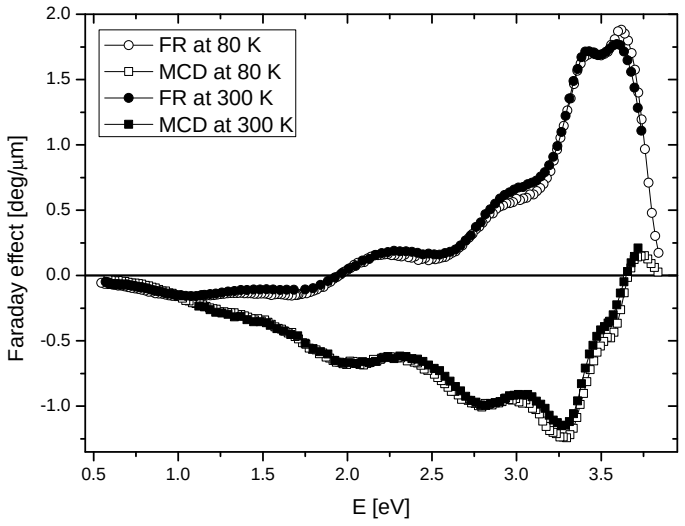

Figure 5.21: Comparison of low and room temperature measurements of Faraday rotation and magnetic circular dichroism of the $Ce_{0.90}Co_{0.10}O_{2-\delta}$ sample. The obtained data are corrected for MgO substrate contribution.

Conclusion

Because of the importance for nowadays research, two groups of magnetic oxides have been investigated and several goals have been set at the beginning of this thesis. The first goal was an investigation of LSMO ultrathin layers with focus on the LSMO/STO interface effects. The second goal was a systematic study of cobalt doped CeO_2 in order to provide thorough description of its optical and magneto-optical properties. Finally the last goal was to introduce the MO spectroscopy as an exceptionally useful and effective method for investigations of ultrathin films and to show its abilities when solving various physical problems.

The LSMO/STO interface phenomena have been properly investigated. Experimental data obtained in MO Kerr effect spectroscopy were confronted with theoretical models based on transfer matrix formalism. Based on these comparisons and previously published results [68, 69, 42] a depth sensitive picture of LSMO layer grown on STO substrate was proposed. This model structure revealed complete suppression of DE interaction in first six monolayers of the LSMO film as a result of preferred e_g $(3z^2 - r^2)$ orbital ordering. In the next three MLs the DE is gradually evolving and at the ninth ML the DE interaction is completely restored when the e_g $(x^2 - y^2)$ orbital ordering is achieved. Such model structure describes the experimental data well, confirming the validity of this proposal. However, the contribution of the fourth to sixth ML to resulting ferromagnetic properties remains questionable although it is believed to be non-zero [42]. At room temperature no contribution of these ML was observed. To possibly provide such information low temperature measurements would be necessary.

The optical and magneto-optical studies of cobalt doped CeO_2 films were studied by means of spectroscopic ellipsometry and MO Faraday spectroscopy. The spectra of diagonal and off-diagonal tensor components were obtained with the help of theoretical models. The diagonal spectra revealed two optical transitions between oxygen and cerium states in agreement with previously published results about pure CeO_2 films [3]. The off-diagonal spectra revealed two paramagnetic transitions involving the cobalt ions. The validity of obtained parameters was confirmed on one hand by a very good agreement between the experimental data of both MO Kerr and Faraday effect and corresponding theoretical models. On the other hand also low temperature Faraday effect measurements were performed. They excluded temperature dependence and confirmed an engagement of the proposed paramagnetic transitions. Therefore a conclusion that the cobalt doping has an essential influence on the resulting ferromagnetic properties of CeO_2 films can be made. The spectroscopic ellipsometry and MO spectroscopy data clearly show increasing absorption and increasing amplitudes of MO effects with increasing cobalt content.

As a final remark we can say that the MO spectroscopy proved itself to be an effective technique in investigation of thin films of these materials. On one hand we saw that it could provide a depth sensitive information. Therefore it helped to obtain a better insight into the orbital structure and mechanisms taking place at the LSMO/STO interface. On the other hand it can be simply used to characterization of MO properties of materials which have not been properly

investigated yet. From this point of view we can use the experimental data of MO spectroscopy to calculate the MO parameters, i.e. the off-diagonal components of the permittivity tensor, as we did in the case of cobalt doped CeO_2 films. The reason why MO spectroscopy is so effective in probing layers on a nanometer scale is its very high sensitivity allowing detection of MO angles with precision of thousandths of degrees.

Bibliography

[1] Anderson, P. W.; Hasegawa, H.: Considerations on Double Exchange. *Physical Review*, vol. 100, no. 2, October 1955: pp. 675–681.

[2] Azzam, R. M. A.; Bashara, N. M.: *Ellipsometry and Polarized Light*. North-Holland Publishing Company, 1977, ISBN 0-7204-0694-3.

[3] Barreca, D.; Bruno, G.; Gasparotto, A.; et al.: Nanostructure and optical properties of CeO_2 thin films obtained by plasma-enhanced chemical vapor deposition. *Materials Science and Engineering: C*, vol. 23, no. 6-8, December 2003: pp. 1013–1016, ISSN 0928-4931.

[4] Belotelov, V. I.; Akimov, I. A.; Pohl, M.; et al.: Enhanced magneto-optical effects in magnetoplasmonic crystals. *Nature Nanotechnology*, vol. 6, no. 6, June 2011: pp. 370–376, ISSN 1748-3387.

[5] Belotelov, V. I.; Bykov, D. A.; Doskolovich, L. L.; et al.: Giant transversal Kerr effect in magneto-plasmonic heterostructures: The scattering-matrix method. *Journal of Experimental and Theoretical Physics*, vol. 110, no. 5, 2010: pp. 816–824, ISSN 1063-7761.

[6] Belotelov, V. I.; Doskolovich, L. L.; Zvezdin, A. K.: Extraordinary Magneto-Optical Effects and Transmission through Metal-Dielectric Plasmonic Systems. *Physial Review Letters*, vol. 98, no. 7, February 2007: p. 077401, ISSN 0031-9007.

[7] Bi, L.; Hu, J.; Jiang, P.; et al.: On-chip optical isolation in monolithically integrated non-reciprocal optical resonators. *Nature Photonics*, vol. 8, no. 5, May 2011: pp. 758–762, ISSN 1749-4885.

[8] Bi, L.; Kim, H.-S.; Dionne, G. F.; et al.: Structural, magnetic, and magneto-optical properties of Co-doped $CeO_{2-\delta}$ films. *Journal of Applied Physics*, vol. 103, no. 7, March 2008: 07D138, ISSN 1089-7550.

[9] Castleton, C. W. M.; Kullgren, J.; Hermansson, K.: Tuning LDA+U for electron localization and structure at oxygen vacancies in ceria. *The Journal of Chemical Physics*, vol. 127, no. 24, December 2007: 244704, ISSN 1089-7690.

[10] Chen, K. R.; Leboeuf, J. N.; Wood, R. F.; et al.: Mechanisms affecting kinetic energies of laser-ablated materials. *Journal of Vacuum Science & Technology A*, vol. 14, no. 3, May 1996: pp. 1111–1114, ISSN 0734-2101.

[11] Chiu, F.-C.; Lai, C.-M.: Optical and electrical characterizations of cerium oxide thin films. *Journal of Physics D: Applied Physics*, vol. 43, no. 7, February 2010: p. 075104, ISSN 0022-3727.

[12] Coey, J. M. D.; Viret, M.; von Molnár, S.: Mixed-valence manganites. *Advances in Physics*, vol. 48, no. 2, 1999: pp. 167–293, ISSN 0001-8732.

[13] Dijkkamp, D.; Venkatesan, T.; Wu, X. D.; et al.: Preparation of Y-Ba-Cu oxide superconductor thin films using pulsed laser evaporation from high T_C bulk material. *Applied Physics Letters*, vol. 51, no. 8, August 1987: pp. 619–621, ISSN 0003-6951.

[14] Eason, R. (editor): *Pulsed Laser Deposition of Thin Films: Applications-Led Growth of Functional Materials*. Hoboken, New Jersey: John Wiley & Sons, second edition, 2007, ISBN 978-0-471-44709-9.

[15] Feiner, L. F.; Oleś, A. M.: Electronic origin of magnetic and orbital ordering in insulating $LaMnO_3$. *Physical Review B*, vol. 59, no. 5, February 1999: pp. 3295–3298, ISSN 1098-0121.

[16] Fernandes, V.; Klein, J. J.; Mattoso, N.; et al.: Room temperature ferromagnetism in Co-doped CeO_2 films on Si(001). *Physical Review B*, vol. 75, no. 12, March 2007: p. 121304, ISSN 1098-0121.

[17] Fontijn, W. F. J.; van der Zaag, P. J.; Feiner, L. F.; et al.: A consistent interpretation of the magneto-optical spectra of spinel type ferrites (invited). *Journal of Applied Physics*, vol. 85, no. 8, April 1999: pp. 5100–5105, ISSN 0021-8979.

[18] Fumagalli, P.; Spaeth, C.; Guntherodt, G.; et al.: Magneto-optic spectroscopy perovskite-type $La_{1-x}(Ba,Sr)_xMnO_3$. *IEEE Transactions on Magnetics*, vol. 31, no. 6, November 1995: pp. 3277–3279, ISSN 0018-9464.

[19] de Gennes, P.-G.: Effects of Double Exchange in Magnetic Crystals. *Physical Review*, vol. 118, no. 1, April 1960: pp. 141–154.

[20] Goodenough, J. B.: Theory of the Role of Covalence in the Perovskite-Type Manganites [La, M(II)]MnO_3. *Physical Review*, vol. 100, no. 2, October 1955: pp. 564–573.

[21] Haghiri-Gosnet, A.-M.; Renard, J.-P.: CMR manganites: physics, thin films and devices. *Journal of Physics D: Applied Physics*, vol. 36, April 2003: pp. R127–R150, ISSN 0022-3727.

[22] Hass, G.; Ramsey, J. B.: Vacuum Deposition of Dielectric and Semiconductor Films by a CO_2 Laser. *Applied Optics*, vol. 8, no. 6, June 1969: pp. 1115–1118, ISSN 1559-128X.

[23] Hauback, B. C.; Fjellvag, H.; Sakai, N.: Effect of Nonstoichiometry on Properties of $La_{1-t}MnO_{3+\delta}$: III. Magnetic Order Studied by Powder Neutron Diffraction. *Journal of Solid State Chemistry*, vol. 124, no. 1, 1996: pp. 43–51, ISSN 0022-4596.

[24] von Helmolt, R.; Wecker, J.; Holzapfel, B.; et al.: Giant negative magnetoresistance in perovskitelike $La_{2/3}Ba_{1/3}MnO_x$ ferromagnetic films. *Physical Review Letters*, vol. 71, no. 14, October 1993: pp. 2331–2333, ISSN 0031-9007.

[25] Huijben, M.; Martin, L. W.; Chu, Y.-H.; et al.: Critical thickness and orbital ordering in ultrathin $La_{0.7}Sr_{0.3}MnO_3$ films. *Physical Review B*, vol. 78, no. 9, September 2008: p. 094413, ISSN 1098-0121.

[26] Hwang, H. Y.; Cheong, S.-W.; Radaelli, P. G.; et al.: Lattice Effects on the Magnetoresistance in Doped $LaMnO_3$. *Physical Review Letters*, vol. 75, no. 5, July 1995: pp. 914–917, ISSN 0031-9007.

[27] Inam, A.; Hegde, M. S.; Wu, X. D.; et al.: As-deposited high T_C and J_C superconducting thin films made at low temperatures. *Applied Physics Letters*, vol. 53, no. 10, September 1988: pp. 908–910, ISSN 0003-6951.

[28] Inoue, M.; Arai, K.; Fujii, T.; et al.: One-dimensional magnetophotonic crystals. *Journal of Applied Physics*, vol. 85, no. 8, April 1999: pp. 5768–5770, ISSN 0021-8979.

[29] Inoue, M.; Fujikawa, R.; Baryshev, A.; et al.: Magnetophotonic crystals. *Journal of Physics D: Applied Physics*, vol. 39, no. 8, April 2006: p. R151, ISSN 0022-3727.

[30] Inoue, M.; Uchida, H.; Nishimura, K.; et al.: Magnetophotonic crystals-a novel magneto-optic material with artificial periodic structures. *Journal of Materials Chemistry*, vol. 16, no. 7, February 2006: pp. 678–684, ISSN 0959-9428.

[31] Iwasaki, K.; Kawai, H.; Suzuki, Y.; et al.: Fabrication and properties of spatial light modulator with magneto-optical Faraday effect. In *Proceedings of SPIE*, vol. 6311, August 2006, p. 631116.

[32] Iwasaki, K.; Mochizuki, H.; Umezawa, H.; et al.: Practical Magneto-Optic Spatial Light Modulator With Single Magnetic Domain Pixels. *IEEE Transactions on Magnetics*, vol. 44, no. 11, November 2008: pp. 3296–3299, ISSN 0018-9464.

[33] Jin, S.; Tiefel, T. H.; McCormack, M.; et al.: Thousandfold Change in Resistivity in Magnetoresistive La-Ca-Mn-O Films. *Science*, vol. 264, no. 5157, April 1994: pp. 413–415, ISSN 0036-8075.

[34] Jonker, G. H.: Semiconducting properties of mixed crystals with perovskite structure. *Physica*, vol. 20, no. 7-12, 1954: pp. 1118–1122, ISSN 0031-8914.

[35] Jonker, G. H.: Magnetic compounds with perovskite structure IV Conducting and non-conducting compounds. *Physica*, vol. 22, no. 6-12, 1956: pp. 707–722, ISSN 0031-8914.

[36] Jonker, G. H.; Van Santen, J. H.: Ferromagnetic compounds of manganese with perovskite structure. *Physica*, vol. 16, March 1950: pp. 337–349, ISSN 0031-8914.

[37] Jung, J. H.; Kim, K. H.; Eom, D. J.; et al.: Determination of electronic band structures of $CaMnO_3$ and $LaMnO_3$ using optical-conductivity analyses. *Physical Review B*, vol. 55, no. 23, June 1997: pp. 15489–15493, ISSN 1098-0121.

[38] Kahn, F. J.; Pershan, P. S.; Remeika, J. P.: Ultraviolet Magneto-Optical Properties of Single-Crystal Orthoferrites, Garnets, and Other Ferric Oxide Compounds. *Physical Review*, vol. 186, no. 3, October 1969: pp. 891–918.

[39] Kodama, T.; Uchida, H.; Baryshev, A.; et al.: Fabrication of three-dimensional magneto-photonic crystal using 450 nm SiO_2 spheres. In *Magnetics Conference, 2005. INTERMAG Asia 2005. Digests of the IEEE International*, April 2005, pp. 2091–2092.

[40] Koubaa, M.; Haghiri-Gosnet, A.; Renard, J.; et al.: Magneto-optical spectroscopy of strained $La_{2/3}Sr_{1/3}MnO_3$ thin films grown by "laser MBE". *Journal of Magnetism and Magnetic Materials*, vol. 272-276, Part 3, 2004: pp. 1812–1813, ISSN 0304-8853, proceedings of the International Conference on Magnetism (ICM 2003).

[41] Kovaleva, N. N.; Oleś, A. M.; Balbashov, A. M.; et al.: Low-energy Mott-Hubbard excitations in $LaMnO_3$ probed by optical ellipsometry. *Physical Review B*, vol. 81, June 2010: p. 235130, ISSN 1098-0121.

[42] Lepetit, M.-B.; Mercey, B.; Simon, C.: Interface Effects in Perovskite Thin Films. *Physical Review Letters*, vol. 108, no. 8, February 2012: p. 087202, ISSN 0031-9007.

[43] Liu, H. L.; Lu, K. S.; Kuo, M. X.; et al.: Magneto-optical properties of $La_{0.7}Sr_{0.3}MnO_3$ thin films with perpendicular magnetic anisotropy. *Journal of Applied Physics*, vol. 99, no. 4, February 2006: 043908, ISSN 0021-8979.

[44] Millis, A. J.; Littlewood, P. B.; Shraiman, B. I.: Double Exchange Alone Does Not Explain the Resistivity of $La_{1-x}Sr_xMnO_3$. *Physical Review Letters*, vol. 74, no. 25, June 1995: pp. 5144–5147, ISSN 0031-9007.

[45] Mistrík, J.; Yamaguchi, T.; Veis, M.; et al.: Magneto-optical and optical spectroscopic ellipsometries of $La_{2/3}Sr_{1/3}MnO_3$ thin films. *Journal of Applied Physics*, vol. 99, April 2006: pp. 08Q317–08Q317–3, ISSN 0021-8979.

[46] Morimoto, Y.; Asamitsu, A.; Kuwahara, H.; et al.: Giant magnetoresistance of manganese oxides with a layered perovskite structure. *Nature*, vol. 380, no. 6570, March 1996: pp. 141–144, ISSN 0028-0836.

[47] Nývlt, M.: *Optical interactions in ultrathin magnetic film structures*. Doctoral Thesis, Charles University, Prague, August 1996.

[48] Ogasawara, T.; Matsubara, M.; Tomioka, Y.; et al.: Photoinduced spin dynamics in $La_{0.6}Sr_{0.4}MnO_3$ observed by time-resolved magneto-optical Kerr spectroscopy. *Physical Review B*, vol. 68, no. 18, Nov 2003: p. 180407, ISSN 1098-0121.

[49] Okimoto, Y.; Katsufuji, T.; Ishikawa, T.; et al.: Variation of electronic structure in $La_{1-x}Sr_xMnO_3$f($0 \leq x \leq 0.3$) as investigated by optical conductivity spectra. *Physical Review B*, vol. 55, no. 7, February 1997: pp. 4206–4214, ISSN 1098-0121.

[50] Park, J. H.; Fujikawa, R.; Kazuhiro, N.; et al.: Fabrication of two dimensional magnetophotonic crystal by selective-area sputter epitaxy. In *Magnetics Conference, 2005. INTERMAG Asia 2005. Digests of the IEEE International*, April 2005, pp. 2089–2090.

[51] Pershan, P. S.: Magneto-Optical Effects. *Journal of Applied Physics*, vol. 38, no. 3, March 1967: pp. 1482–1490, ISSN 0021-8979.

[52] Pickett, W. E.; Singh, D. J.: Electronic structure and half-metallic transport in the $La_{1-x}Ca_xMnO_3$ system. *Physical Review B*, vol. 53, no. 3, January 1996: pp. 1146–1160, ISSN 1098-0121.

[53] Pohl, M.; Kreilkamp, L. E.; Belotelov, V. I.; et al.: Tuning of the transverse magneto-optical Kerr effect in magneto-plasmonic crystals. *New Journal of Physics*, vol. 15, no. 7, July 2013: p. 075024, ISSN 1367-2630.

[54] Prellier, W.; Lecoeur, P.; Mercey, B.: Colossal-magnetoresistive manganite thin films. *Journal of Physics: Condensed Matter*, vol. 13, November 2001: pp. R915–R944, ISSN 0953-8984.

[55] Ramirez, A. P.: Colossal magnetoresistance. *Journal of Physics: Condensed Matter*, vol. 9, no. 39, September 1997: pp. 8171–8201, ISSN 0953-8984.

[56] Rao, C. N. R.; Arulraj, A.; Cheetham, A. K.; et al.: Charge ordering in the rare earth manganates: the experimental situation. *Journal of Physics: Condensed Matter*, vol. 12, no. 7, February 2000: p. R83, ISSN 0953-8984.

[57] Rauer, R.; Neuber, G.; Kunze, J.; et al.: Magneto-optical investigation of spin polarisation of $La_{0.7}Ca_{0.3}MnO_3$ and $La_{0.7}Sr_{0.3}MnO_3$. *Journal of Magnetism and Magnetic Materials*, vol. 290-291, Part 2, 2005: pp. 948–951, ISSN 0304-8853, proceedings of the Joint European Magnetic Symposia (JEMS' 04).

[58] Ritter, C.; Ibarra, M. R.; De Teresa, J. M.; et al.: Influence of oxygen content on the structural, magnetotransport, and magnetic properties of $LaMnO_{3+\delta}$. *Physical Review B*, vol. 56, no. 14, October 1997: pp. 8902–8911, ISSN 1098-0121.

[59] Rodríguez-Carvajal, J.; Hennion, M.; Moussa, F.; et al.: Neutron-diffraction study of the Jahn-Teller transition in stoichiometric $LaMnO_3$. *Physical Review B*, vol. 57, no. 6, February 1998: pp. R3189–R3192, ISSN 1098-0121.

[60] Sakai, N.; Fjellvag, H.; Lebech, B.: Effect of Non-Stoichiometry on Properties of $La_{1-t}MnO_{3+\delta}$. Part II. Crystal Structure. *Acta Chemica Scandinavica*, vol. 51, 1997: pp. 904–909, ISSN 0904-213X.

[61] Salamon, M. B.; Jaime, M.: The physics of manganites: Structure and transport. *Reviews of Modern Physics*, vol. 73, no. 3, August 2001: pp. 583–628, ISSN 0034-6861.

[62] Shintaku, T.: Integrated optical isolator based on efficient nonreciprocal radiation mode conversion. *Applied Physics Letters*, vol. 73, no. 14, October 1998: pp. 1946–1948, ISSN 0003-6951.

[63] Slusser, P. K.: *Transition metal doped cerium oxide for spintronics applications*. Master's Thesis, University of Utah, August 2009.

[64] Smith, H. M.; Turner, A. F.: Vacuum Deposited Thin Films Using a Ruby Laser. *Applied Optics*, vol. 4, no. 1, January 1965: pp. 147–148, ISSN 1559-128X.

[65] Sobu, Y.; Shoji, Y.; Sakurai, K.; et al.: GaInAsP/InP MZI waveguide optical isolator integrated with spot size converter. *Optical Express*, vol. 21, no. 13, July 2013: pp. 15373–15381, ISSN 1094-4087.

[66] Sun, J. Z.; Abraham, D. W.; Rao, R. A.; et al.: Thickness-dependent magnetotransport in ultrathin manganite films. *Applied Physics Letters*, vol. 74, no. 20, May 1999: pp. 3017–3019, ISSN 0003-6951.

[67] Takenaka, K.; Iida, K.; Sawaki, Y.; et al.: Optical Spectra Measured on Cleaved Surfaces of Double-Exchange Ferromagnet $La_{1-x}Sr_xMnO_3$. *physica status solidi (b)*, vol. 215, no. 1, September 1999: pp. 637–641, ISSN 1521-3951.

[68] Tebano, A.; Aruta, C.; Sanna, S.; et al.: Evidence of Orbital Reconstruction at Interfaces in Ultrathin $La_{0.67}Sr_{0.33}MnO_3$ Films. *Physical Review Letters*, vol. 100, no. 13, April 2008: p. 137401, ISSN 0031-9007.

[69] Tebano, A.; Orsini, A.; Medaglia, P. G.; et al.: Preferential occupation of interface bands in $La_{2/3}Sr_{1/3}MnO_3$ films as seen via angle-resolved photoemission. *Physical Review B*, vol. 82, no. 21, December 2010: p. 214407, ISSN 1098-0121.

[70] Tiwari, A.; Bhosle, V. M.; Ramachandran, S.; et al.: Ferromagnetism in Co doped CeO_2: Observation of a giant magnetic moment with a high Curie temperature. *Applied Physial Letters*, vol. 88, no. 14, April 2006: 142511, ISSN 1077-3118.

[71] Tobe, K.; Kimura, T.; Okimoto, Y.; et al.: Anisotropic optical spectra in a detwinned $LaMnO_3$ crystal. *Physical Review B*, vol. 64, no. 18, October 2001: p. 184421, ISSN 1098-0121.

[72] Tokura, Y.; Tomioka, Y.: Colossal magnetoresistive manganites. *Journal of Magnetism and Magnetic Materials*, vol. 200, no. 1-3, October 1999: pp. 1–23, ISSN 0304-8853.

[73] Uba, L.; Uba, S.; Germash, L. P.; et al.: Electronic structure and magneto-optical spectra of $La_xSr_{1-x}MnO_3$ perovskites: Theory and experiment. *Physical Review B*, vol. 85, no. 12, March 2012: p. 125124, ISSN 1098-0121.

[74] Van Santen, J. H.; Jonker, G. H.: Electrical conductivity of ferromagnetic compounds of manganese with perovskite structure. *Physica*, vol. 16, July–August 1950: pp. 599–600, ISSN 0031-8914.

[75] Veis, M.: *Optical interactions in thin films of selected magnetic oxides*. Doctoral Thesis, Charles University, Prague, March 2009.

[76] Veis, M.; Višňovský, Š.; Lecoeur, P.; et al.: Magneto-optic spectroscopy of $La_{2/3}Sr_{1/3}MnO_3$ films on $SrTiO_3$ (100) and (110) substrates. *Journal of Physics D: Applied Physics*, vol. 42, no. 19, September 2009, ISSN 0022-3727.

[77] Veis, M.; Zahradnik, M.; Antos, R.; et al.: Interface effects and the evolution of ferromagnetism in $La_{2/3}Sr_{1/3}MnO_3$ ultrathin films. *Science and Technology of Advanced Materials*, vol. 15, no. 1, February 2014: p. 015001, ISSN 1468-6996.

[78] Višňovský, Š.: Magneto-optical ellipsometry. *Czechoslovak Journal of Physics B*, vol. 36, no. 5, May 1986: pp. 625–650, ISSN 0011-4626.

[79] Višňovský, Š.: *Optics in Magnetic Multilayers and Nanostructures*. Taylor & Francis Group, 2006, ISBN 978-0-8493-3686-4.

[80] Vodungbo, B.; Zheng, Y.; Vidal, F.; et al.: Room temperature ferromagnetism of Co doped $CeO_{2-\delta}$ diluted magnetic oxide: Effect of oxygen and anisotropy. *Applied Physics Letters*, vol. 90, no. 6, February 2007: 062510, ISSN 0003-6951.

[81] Wang, J.; Hu, F. X.; Li, R. W.; et al.: Strong tensile strain induced charge/orbital ordering in (001)-$La_{7/8}Sr_{1/8}MnO_3$ thin film on 0.7Pb($Mg_{1/3}Nb_{2/3}$)O_3-0.3$PbTiO_3$. *Applied Physics Letters*, vol. 96, no. 5, February 2010: 052501, ISSN 1077-3118.

[82] Wollan, E. O.; Koehler, W. C.: Neutron Diffraction Study of the Magnetic Properties of the Series of Perovskite-Type Compounds [$(1-x)$La, xCa]MnO_3. *Physical Review*, vol. 100, no. 2, October 1955: pp. 545–563.

[83] Yamaguchi, S.; Okimoto, Y.; Ishibashi, K.; et al.: Magneto-optical Kerr effects in perovskite-type transition-metal oxides: $La_{1-x}Sr_xMnO_3$ and $La_{1-x}Sr_xCoO_3$. *Physical Review B*, vol. 58, no. 11, September 1998: pp. 6862–6870, ISSN 1098-0121.

[84] Yeh, P.: Optics of anisotropic layered media: A new 4×4 matrix algebra. *Surface Science*, vol. 96, June 1980: pp. 41–53, ISSN 0039-6028.

[85] Zahradník, M.: *Magnetooptical spectroscopy of $La_{2/3}Sr_{1/3}MnO_3$ ultrathin films*. Bachelor's Thesis, Charles University, Prague, 2012.

[86] Zener, C.: Interaction between the d-Shells in the Transition Metals. II. Ferromagnetic Compounds of Manganese with Perovskite Structure. *Physical Review*, vol. 82, 1951: pp. 403–405.

List of Abbreviations

CF	-	crystal field
CT	-	charge transfer
CMR	-	colossal magnetoresistance
DE	-	double-exchange
FR	-	Faraday rotation
KE	-	Kerr ellipticity
KR	-	Kerr rotation
LSMO	-	$La_{2/3}Sr_{1/3}MnO_3$
MBE	-	molecular beam epitaxy
MCD	-	magnetic circular dichroism
ML(s)	-	monolayer(s)
MO	-	magneto-optical
MOCVD	-	metalorganic chemical vapour deposition
MOKE	-	magneto-optical Kerr effect
MRAM	-	magnetoresistive random-access memory
PLD	-	pulsed laser deposition
RT	-	room temperature
SE	-	spectroscopic ellipsometry
STO	-	$SrTiO_3$
UV	-	ultraviolet